Objectively-Derived Daily "Winds" From Satellite Scatterometer Data

by

P. J. Pegion, M. A. Bourassa, D. M. Legler, and J. J. O'Brien

Center for Ocean-Atmospheric Prediction Studies
Florida State University
Tallahassee, Florida 32306, USA

Monthly Weather Review

Corresponding author: Mark A. Bourassa

Center for Ocean-Atmospheric Prediction Studies
Florida State University
Tallahassee, Florida 32306, USA
bourassa@coaps.fsu.edu
Phone: (850) 644-6923
FAX: (850) 644-4841

ABSTRACT

An objective technique is used to create regularly gridded daily “wind” fields from NASA scatterometer (NSCAT) observations for the Pacific Ocean north of 40°S. The objective technique is a combination of direct-minimization, and cross validation with multigridding. The fields are created from the minimization of a cost function. The cost function is developed to maximize information from the observational data and minimize smoothing. Three constraints are in the cost function: a misfit to observations, a smoothing term, and a misfit of curl. The second and third terms are relative to a background field. The influence of the background field is controlled by weights on the smoothing constraints. Weights are objectively derived by the method of cross validation. Cross validation is a process that removes observations from the input to the cost function and determines tuning parameters (weights) by the insensitivity of the removed observations to the output field. This method is computationally expensive; thus the technique of multigridding is incorporated into cross validation. Multigridding solves for the weights by cross validation on a coarse grid, then these weights are used to determine pseudostress on the original fine grid. This allows for the practical application of cross validation with only modest computational resources required.

Daily pseudostress fields are generated on a 1° by 1° resolution grid for the NSCAT period. These objectively derived fields are compared to independent data sources (NCEP and FSU Winds). The kinetic energy of the NSCAT fields exceeds that of the independent NCEP reanalysis and is similar to observations. Pseudostresses for the equatorial cold tongue region (15°S to 15°N, 180° to 90°W) are extracted from the objectively derived NSCAT fields and a Complex Empirical Orthogonal Function (CEOF) analysis is performed. The analysis shows a large amount of variability in intra-seasonal time-scales for the Southern Hemisphere tradewinds. This variability is supported by in-situ observations.

1. INTRODUCTION

The NASA scatterometer (NSCAT; Naderi et al. 1991) operated for only 9.5 months, but provided an unprecedented quantity of high quality wind data over the oceans. NSCAT was an active microwave radar mounted on a polar orbiting satellite that retrieved high-resolution surface (10 m) wind vectors. Wind speed and direction were measured for ~77% of the ice-free oceans each day. This high spatial coverage was made possible by two sets of antennae, one on each side of the satellite relative to the forward motion, which allowed for two swaths of ocean to be observed simultaneously. Accuracy and spatial coverage of these observations were unprecedented (Bourassa et al. 1997; Caruso et al. 1999; Freilich and Dunbar 1999). Despite the high quality and excellent coverage that NSCAT data provided, the data contain spatial gaps that need to be filled before these observations can be easily utilized for forcing ocean models (Kelley et al. 1999; Milliff et al. 1999b; Verschell et al. 1999) or for studies of atmospheric variability (Bourassa et al. 1999; Chelton et al. 2000a,b; Chen et al. 1999; Milliff et al. 1999a). Such gridded fields revealed previously unobserved behaviors in gap flow (Bourassa et al. 1999), and lead to better understanding of the physical mechanisms responsible for flow through Central American passes (Chelton et al. 2000a,b). For such purposes, serially complete daily pseudostress fields based purely on NSCAT data are desirable. This study details a new approach to produce these fields.

Other wind products over the ocean are available; however they are not based on NSCAT data. Ships and buoys collect an order of magnitude fewer observations than NSCAT did. Furthermore, most of these observations were taken in shipping lanes, leaving large portions of the ocean unobserved. Also, ship observations have large errors (Pierson 1990) in speed and direction. Nevertheless, in-situ observations have demonstrated value in producing monthly products, such as the specialized tropical wind products (Servain et al. 1996; Stricherz et al. 1997; Legler et al. 1997).

Surface winds are also available from atmospheric general circulation models such as the National Centers for Environmental Prediction – National Center for Atmospheric Research (NCEP–NCAR) reanalysis (Kalnay et al. 1996). The reanalysis data have a much coarser spatial resolution than NSCAT data and are noted to have a poor handling of the wind field in equatorial regions (Putman et al. 2000).

Other remote sensing devices have retrieved surface winds over the ocean. Special Sensor Microwave/Imager (SSM/I; Atlas et al. 1996) and altimeters (Chelton and Wentz 1986) can only measure wind speed. The European Space Agency’s European Remote Sensing satellite (ERS-1/2) scatterometers measured both speed and direction, but the rate at which data can be collected is less than half of NSCAT. The dearth of data collected by ERS-1/2 is due to the relatively narrow single swath of ocean that is observed (unlike NSCAT, which measured two swaths) and operational constraints. However, some products are available (Bentamy et al. 1996; Siefridt et al. 1998)

NSCAT data are an improvement on all of the previously mentioned sources of wind vector data, but gaps between the observational swaths and sampling problems limit the usefulness. Poor sampling has greatly limited the utility of ERS-1/2 observations (Legler and O'Brien 1985; Zeng and Levy 1995; Schlax et al. 2000). Several techniques have been attempted to deal with these problems for NSCAT products. Tang and Liu (1996) used European Centre for Medium–Range Weather Forecasts (ECMWF) winds to fill the gaps, and they applied objective interpolation. The need for non-NSCAT data was eliminated in various interpolation approaches (Polito et al. 1997; Bentamy et al. 1996, 1998). Interpolation schemes such as these suffered from the obvious appearance of the satellite tracks in spatial derivative fields (i.e., vorticity and divergence). Alternative approaches use weighted spatial and/or temporal averages (Bourassa et al. 1998; Kutsuwada 1998; Bourassa et al. 1999; Kelly et al. 1999). These approaches suffer from excessive smoothing and reduction of kinetic energy in the wind field due to the averaging. Another approach (Chin et al. 1998), which removes satellite tracks, applied wavelet-based multi-resolution analysis to a combination of NSCAT, ERS-2, and NCEP winds. The averaging techniques reduce the problems with the satellite tracks; however, they have excessive smoothing. The new technique discussed in this paper is effective in removing the satellite tracks signature with a minimal amount of smoothing.

The method for filling the observational gaps used herein is direct-minimization. This approach applies several constraints to maximize similarity to observations and minimize non-geophysical features in the spatial derivatives, particularly the satellite tracks in the curl field. Previous works (Legler et al. 1989; Meyers et al. 1994; Siefridt et al. 1998) have shown that three constraints can be coupled to construct smooth wind fields. Each of these constraints is multiplied by a weight. In previous studies, these weights have been determined through subjective observations (Legler et al. 1989), or less subjectively through a sensitivity study (Meyers et al. 1994). Here, a technique (cross validation) is applied to objectively determine these weights.

The NSCAT data and a gridded NSCAT product are detailed in section 2. The methodology of direct-minimization and cross validation is described in section 3. Spatial dependence of the weights is investigated in section 4 and is shown to be minimal. Weights are determined by cross validation and are used to create 1° resolution daily pseudostress fields for the Pacific Ocean from 40°S to 60°N and from 105°E to 65°W.

The objectively derived daily NSCAT pseudostress fields are compared (section 4) to the FSU Winds (Stricherz et al. 1997) and the NCEP reanalysis (Kalnay et al. 1996). Pseudostress data from the region around the equatorial cold tongue in the eastern Pacific Ocean are extracted for a Complex Empirical Orthogonal Function analysis (CEOF; Section 4). The first four CEOF modes, which contain 43.3% of the total variance, are statistically significant. Mode 1 represents the seasonal cycle of the tradewinds. Modes 2 and 4 show synoptic variability in the western portion of the region and around the Gulf of Tehuantepec. The third mode is representative of the South Pacific Convergence Zone (SPCZ).

2. DATA

The Pacific Ocean from 40°S to 60°N and from 105°E to 65°W was chosen as the region to generate objectively derived NSCAT daily pseudostress fields. NSCAT data began on September 15, 1996, and ended on June 29, 1997, with the demise of the Advanced Earth Observing Satellite (ADEOS). These nine and a half months are referred to as the NSCAT period.

Although NSCAT backscatter is interpreted as winds, pseudostresses are chosen rather than winds because the resulting gridded NSCAT data product is intended for ocean modeling.

Ocean circulation is largely driven by wind stress and the curl of wind stress. Wind stress is extremely difficult to measure, but can be approximated by a bulk aerodynamic approach. This approach defines the zonal (τ_x) and meridional (τ_y) components of the wind stress as:

$$\tau_x = \rho C_D u \text{ and } \tau_y = \rho C_D v, \tag{1}$$

where ρ is the density of air and C_D is the drag coefficient. The zonal (*u*) and meridional (*v*) components of the pseudostress are defined as:

$$u = Uu' \text{ and } v = Uv', \tag{2}$$

where U is the wind speed; u' and v' are the zonal and meridional components of the wind vector.

a. NSCAT Observations

A scatterometer is an active radar that emits a beam of microwave radiation directed towards the sea-surface. The scatterometer measures backscatter, which is the amount of microwave energy that returns to the satellite from the sea surface. The amount of backscatter is dependent on the roughness of the sea surface, which can be related empirically to wind speed. Direction is determined by multiple scans of the same spot on the sea surface from different angles. Three scatterometer antennae on each side of the satellite point in different directions. The motion of the satellite allows the same spot to be viewed from three different angles over a relatively short period of time.

NSCAT observations had a spatial grid spacing of approximately 25 km. The scatterometer measured a swath of ocean on each side of the satellite parallel to its motion. Each swath was 600 km wide and there was a 400 km ‘nadir gap’ between the swaths (Fig. 1). Wind speed and direction was measured at this high resolution resulting in ~550,000 ocean vector wind observations per day.

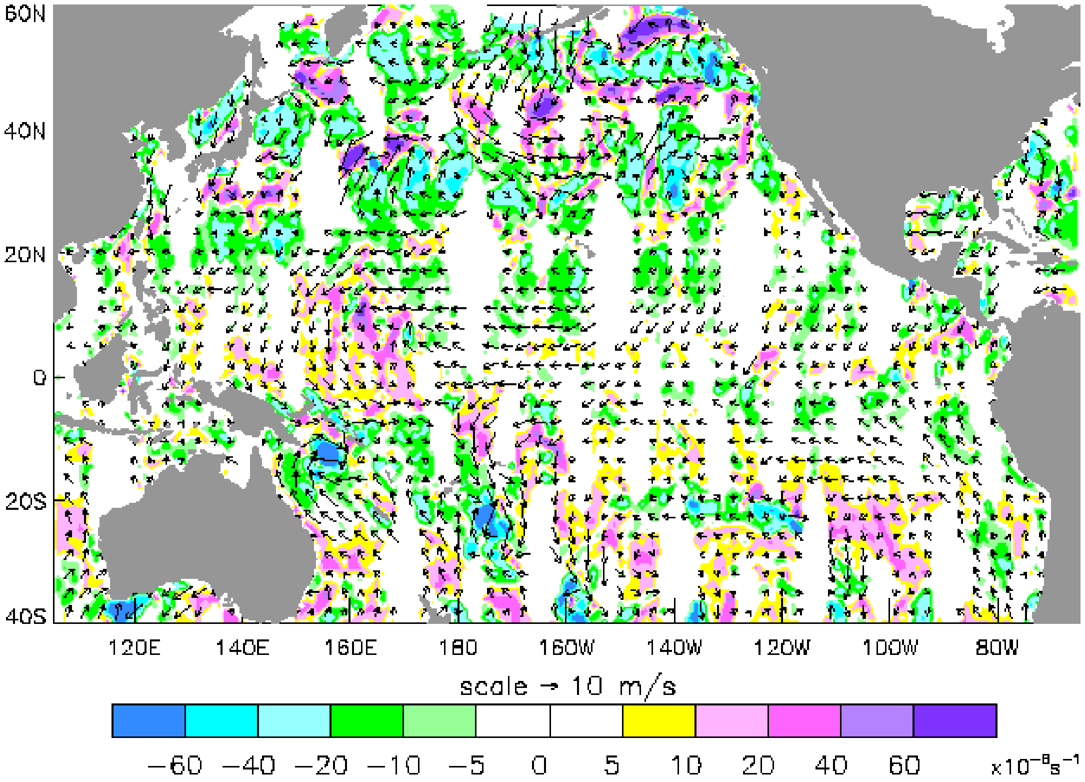

FIG. 1. 24 hours (May 15, 1997) of NSCAT observations for the Pacific Ocean basin north of 40°S. Observation are binned into a 1° by 1° grid. Vorticity is contoured, and wind vectors are plotted every 3° by 3° for clarity. Gaps in the daily coverage are clearly seen.

A wide range of in-situ observations was used to validate NSCAT wind vectors. Buoys (Graber et al. 1997; Atlas et al. 1999), research vessels (Bourassa et al. 1997), quality controlled buoys (Freilich and Dunbar 1999), and volunteer observing ships (Atlas et al. 1999) show that NSCAT observations are highly accurate. Comparison were also made with remotely sensed winds and analyses from the NCEP, Goddard Earth Observing System (GEOS), and ECMWF models (Atlas et al. 1999). The accuracy in speed is ~1.2 ms^{-1} (Freilich and Dunbar 1999). The accuracy in direction is 13° for correctly chosen ambiguities (Bourassa et al. 1997) with ~90% correct selection of ambiguities (Gonzales and Long 1999). These estimates of accuracy are preliminary estimates that ignore uncertainty in the truth, and therefore must be considered upper limits.

b. Background Field

The COAPS/NSCAT temporally-weighted winds (Bourassa et al. 1999) are used as the background fields for direct-minimization because this data set consists of purely NSCAT winds. This data set is an eight-day weighted temporal average of NSCAT wind vectors on a 1° by 1° grid. Wind vectors for each grid cell are averaged with more weight placed on the days closer to the day of interest. The weakness of the temporally-weighted winds is an excessive smoothing, which reduces the anomalies of transient or moving features. These fields have the virtue of relatively little appearance of edge effects along the observational swaths and gaps in daily coverage. This is an essential characteristic of the background field, otherwise these problems will transferred to the solution field.

3. METHODOLOGY

Daily 1°x1° NSCAT pseudostress fields are generated using a technique that involves direct-minimization of a cost function. Development of the cost function is described in section 3*a*. Associated with each term in the cost function is a weight, which is objectively derived through the method of cross validation (section 3*b*). Cross validation is computationally expensive, therefore the technique of multigridding (section 3*c*) is implemented to reduce computation time.

a. Direct-Minimization

Direct-minimization (Fig. 2) requires the creation of a cost function to be minimized. The cost function herein utilizes the information from the observations while forcing the solution field to be smooth with respect to the background field.

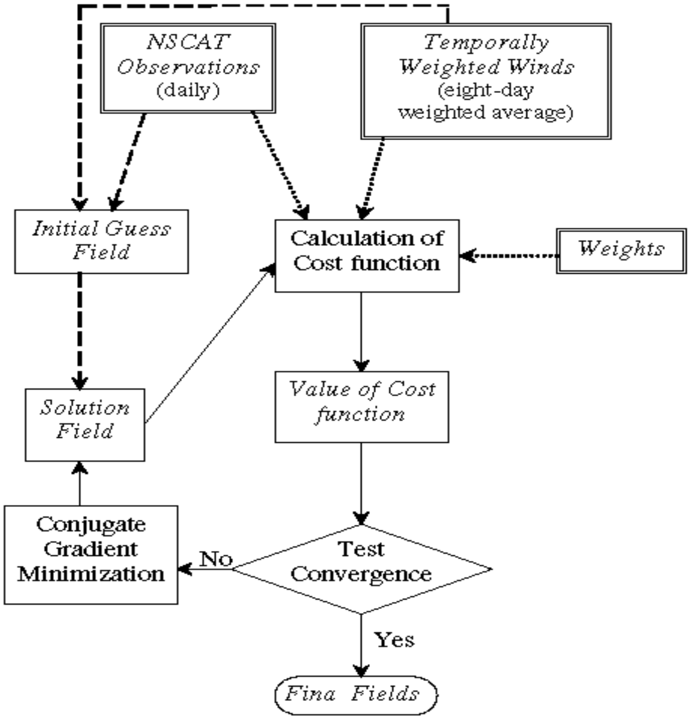

FIG. 2. Flow chart for Direct-Minimization. Italics indicate numerical values or results, boxes with double-lined borders indicate input values. Dashed lines indicate a single (initial) use

of the input data, and dotted lines indicate repeated use of the input data. There are ~250,000 NSCAT vector wind observations in the study region for each day (~550,000 globally), and ~14,000 water grid points (or ~33,000 globally) for 1° grid spacing. The conjugate gradient method requires the derivative of the functional, for each of these grid points, with respect to both components of the pseudostress vector, for typically eight to ten iterations

Previous work (Legler et al. 1989; Meyers et al. 1994; Siefridt et al. 1998) showed that three constraints are necessary for a vector field. These constraints are: a misfit to observations, a Laplacian smoothing term or penalty function, and a kinematic constraint (misfit of the curl of the pseudostress). The cost function (*f*) developed to find the solution vector pseudostress (*u, v*) is:

$$f = \sum_{i,j}^{I,J} \Big\{ \ln(1 + N_{i,j}) \Big[\big(u_{i,j} - u_{o_{i,j}}\big)^2 + \big(v_{i,j} - v_{o_{i,j}}\big)^2 \Big] + \beta_a L^4 \Big[\Big(\nabla^2 \big(u_{i,j} - u_{bg_{i,j}}\big)\Big)^2 + \Big(\nabla^2 \big(v_{i,j} - v_{bg_{i,j}}\big)\Big)^2 \Big]$$

$$+ \beta_b L^2 \Big[\hat{k} \bullet \nabla \times \big(\vec{u}_{i,j} - \vec{u}_{bg_{i,j}}\big)\Big]^2 \Big\}; \qquad (3)$$

where *i* and *j* are indices for the longitude and latitude, and *I* and *J* are the number of longitudinal and latitudinal grid points. The subscript '*o*' indicates NSCAT observations and the subscript '*bg*' is the background field of pseudostress (temporally-weighted NSCAT winds), $\vec{u}$ is the vector pseudostress. The pseudostress components without a subscript are the solution. The second and third terms are scaled by a length scale *L*, which is chosen to be the distance between grid points at the equator. The number of observations at each grid point ($N_{i,j}$) in the first term of (3) is used to emphasize the reduced uncertainty of the mean observations in cells with greater numbers of observations. Grid points that have no NSCAT observations have the first term of the cost function set to zero by $N_{i,j}$. The two weights (β_a and β_b) govern the contribution of the smoothing terms to the cost function. The Laplacian and curl terms link the value at one grid point to surrounding grid points to ensure spatial continuity of the field.

This equation is solved for a minimum in the cost function (*f*). The minimization of this non-linear least squares equation is accomplished iteratively through conjugate minimization (Shanno and Phua 1980). A first guess for the solution fields is made from NSCAT observations binned onto a 1° grid, centered around the grid points, with data from the background field filling missing points. Before the cost function can be minimized, the two free weights must be determined.

b. Cross Validation

The objective calculation of the weights for direct-minimization is done by cross validation. Generalized cross validation (GCV; Wahba and Wendelberger 1980) is not a new technique in other scientific fields; however GCV has only recently been used in meteorological applications. One application of GCV in meteorology is to measure the uncertainty and quality in a forecasting algorithm (Elsner and Schmertmann 1994). In another study, Michaelsen (1987) masked (removed) observations from the forecasting algorithm and determined the importance an observation has in the forecast. A second application for GCV is for fitting a surface of some unknown order to available data. This second application of GCV is used in determining the weights for direct-minimization.

Cross validation (Fig. 3) finds the weights for direct-minimization by removing observations from the calculation of the cost function and comparing this result to the case when no observations are masked. The differences of many such pairs are minimized, in a least squares sense, with respect to the weights.

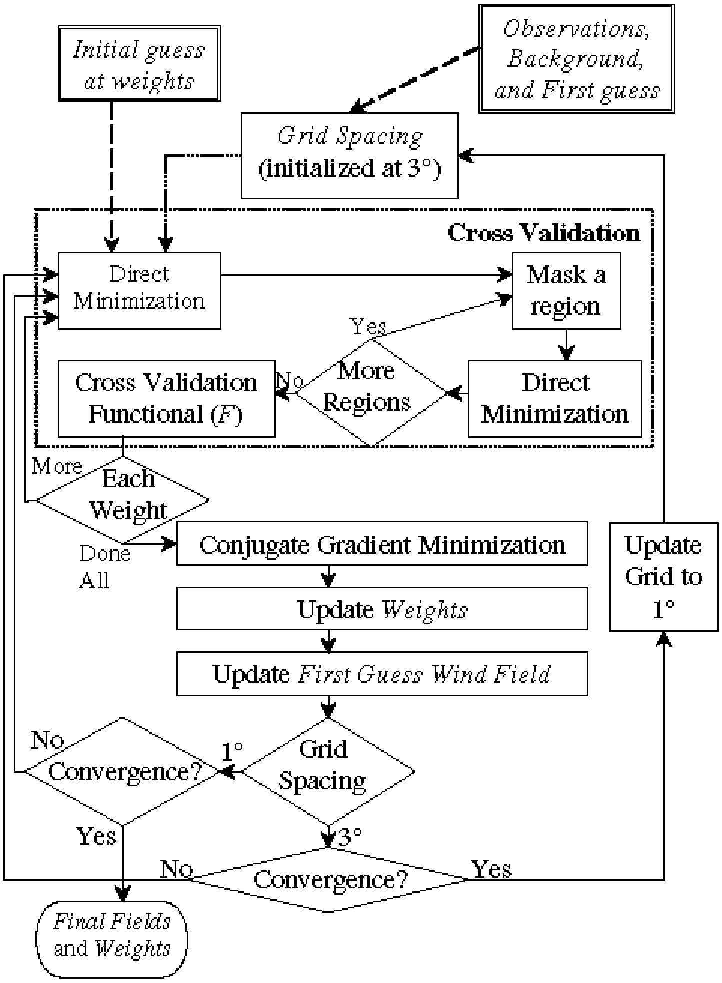

Fig. 3. Flow chart for cross validation and multigridding. Lines and boxes are as for Fig. 2, and the dotted box contains the cross validation procedure. Cross validation must be applied to each weight, typically for six to eight iterations on the coarse grid, and then for one more adjustment on the fine grid. Calculation of the cross validation functional requires $2K+1$ calculations of the direct minimization functional, where K is the number of masked regions.

The cross validation functional (*F*)

$$F(\beta) = \sum_{k}^{K} \left(f_k(\beta) - \tilde{f}(\beta) \right)^2, \tag{4}$$

is designed to minimize the difference between the cost function (eq. 3) without data exclusion ($\tilde{f}$) and the cost function with data exclusion (f_k). The number, *K*, is the number of masked subsets, and β is the vector of weights. This approach finds weights, which optimize *f* for the constraints in (3), and for which small variations in the weights have little impact on the fields. This simple form of *F* is effective because the minimum values of $f(\beta)$ correspond to minima in the sensitivity of *F* to β (Meyers et al. 1994).

The weights associated with a minimum in *F* are determined through conjugate minimization. Direct-minimization requires positive values for the weights; however, the conjugate gradient method allows solutions to range from $-\infty$ to ∞ . The natural log of the weights is utilized to meet these requirements. The derivative of the functional with respect to the natural log of the weights is:

$$\frac{dF}{d\ln(\beta)} \cong 2\sum_{k}^{K} \left[\left(f_k - \tilde{f} \right) \left(\frac{\Delta f_k}{\Delta \ln(\beta)} - \frac{\Delta \tilde{f}}{\Delta \ln(\beta)} \right) \right]. \tag{5}$$

The first constraint in $\tilde{f}$ (the cost function) is dependent on the number of grid points with observations, the value of f_k changes when regions are masked. A correction is needed to scale the first constraint in f_k; otherwise the misfit to observations in f_k will be biased low compared to $\tilde{f}$. This scaling is:

$$r = \frac{\tilde{N}}{N_k}. \tag{6}$$

where $\tilde{N}$ is the number of grid cells with observations in $\tilde{f}$, and N_k is the number of grid cells with observations in f_k. Scaling by this ratio reduces a bias in the gradient used to find the weights. The weights are found by setting (5) equal to zero and solving this non-linear least squares problem using an iterative method. This approach requires a first guess for the weights; however, the result is independent for guesses within at least ±3 orders of magnitude.

Cross validation requires the removal of independent observations; otherwise the information associated with the masked observation is never fully removed from the calculation. Subsets of data are excluded due to the fact that meteorological variables are closely correlated in space. The subsets need to be large enough so the center point of the subset is independent from the points that remain for cross validation. A 12° latitude by 12° longitude mask is expected to be more than large enough (Chelton and Wentz 1986).

The size of the study area and the size of the mask limit the maximum number of masked regions. In practice, these masked regions must cover a wide range of wind regimes in the study area. This is necessary because even though the weights are assumed to be spatially independent, different wind patterns and different vorticity fields need to be examined to determine the best weight for the entire region. For this study area, the uncertainty in the weights decreases as the number of excluded regions increases. Sixteen masked regions provide reasonable coverage over the study region, while calculating optimal weights with substantially fewer regions (e.g. 12) results in the weights varying more than an order of magnitude. There are 14,321 points where the functional is calculated and only about 2,200 points have observations masked. With fewer masked regions, there are large areas of observations that are not considered in the cross validation. These areas tend to occur in the tropics due to the constraint that each masked region needs to have observations in 90% of the grid cells. The geometry of the satellite orbit results in relatively few locations in the tropics where there are such 12° by 12° bins.

The computational requirements for cross validation could be greatly reduced by determining changes to the field contributing to f_k only in the area of a masked region (R. Hoffman, 1999, personal communication). Such an approach was not used herein; however, for this study region, the number of computations is conservatively estimated to be reduced by a factor of 15. Further studies will more accurately determine the advantages of this approach. Combined with the computational reductions due to multigridding (discussed below), it will be practical to determine optimal weights for global daily gridded fields in near real-time.

c. Multigridding

Cross validation requires about 15 CPU-hours on a SGI Origin 2000 with 200 MHz processors to determine the optimal weights for one daily pseudostress field. An increase in efficiency is needed to make cross validation practical. The weights that are determined by cross validation are expected to be independent of space. This suggests that the weights found for a coarse grid will be valid for a finer grid. A coarse grid has fewer points for calculations, allowing much faster results. The technique of multigridding (Brandt 1982) calculates the optimal weights through cross validation on a coarse grid, then uses these optimal weights as the initial guess on the fine (1° by 1°) grid, and one adjustment (i.e., one correction through the conjugate gradient method) on the fine grid adequately tunes the weights.

The method of multigridding is valid only if the solutions from two different grid spacings are within an order of magnitude (Brandt 1982). This requirement is validated with calculations of optimal weights on 1°, 2°, 3°, and 6° grids for several test cases; one test case is presented in table 1. The optimal weights vary within an order of magnitude; therefore multigridding is a valid technique for this study.

The size of the masked subset regions dictates the grid spacing of the coarse grid. The masked region size must be an even integer multiple of the coarse grid spacing. A 1° by 1° fine grid is used here, and the masked regions are 12° by 12° squares. This geometry allows for 2°, 3°, and 6° coarse grids. Weights calculated on the 6° grid have variability much larger than the weights from the finer grids and were determined to be unstable. The 2° and 3° grids are stable and the 3° grid is chosen for minimization of computer time use, resulting in approximately a factor of nine reduction in processing time.

4 RESULTS

a. Verification of optimal weights

Visual inspection of the output fields provides a preliminary verification that cross validation chooses the optimal weights correctly. Fields constructed with weights that are too low have vorticity fields that show satellite tracks. Conversely, weights that are too high result in fields with too much smoothing, and details that are in the observations are lost. The effectiveness in which NSCAT observations are preserved is shown quantitatively in the comparison of the average kinetic energy of the 1° by 1° binned swath data (observations), output, and background fields. Kinetic energy is defined as $0.5mU^2$, where m is mass and U is speed. The density of the surface air has a negligible amount of variability compared to the variability of wind, thus mass is neglected in this comparison, and specific kinetic energy is represented by the square of the wind speed (which is equal to the magnitude of the pseudostress). The average kinetic energy for one day (May 15, 1997) in the study region (40°S-60°N, 105°E-65°W) is 22.1 m^2s^{-2} for NSCAT observation, 21.5 m^2s^{-2} for the resultant field, and 17.6 m^2s^{-2} for the background field. Since little kinetic energy is lost in the resultant field compared to the observations, it is clear that the weights for the smoothing terms in the cost function are not too high. Furthermore, the vorticity field does not show the satellite tracks which are apparent in the first guess field.

1) Spatial independence of optimal weights

Cross validation assumes that the weights are independent of space and magnitude of the pseudostress. Spatial independence is tested by calculating optimal weights for two smaller regions of the Pacific Ocean. One sub-region is the mid-latitude north Pacific (30°N -60°N, 125°E- 105°W). This region is characterized by strong winds and high vorticity. The other sub-region is the equatorial western Pacific (20°S - 20°N, 115°E - 165°E) and is selected because it has low wind speeds. The differences in the weights between these two sub-regions and the weights for the entire Pacific Ocean are small (Table 2). Pseudostress fields created from these different sets of weights show little sensitivity to the weights. The change in the output field due to the different weights is typically less than 4.7 m^2s^{-2} (0.5 ms^{-1}), which is near the uncertainty of the binned NSCAT observations, and verifies that the weights are nearly independent of space and magnitude.

2) Time dependence of optimal weights

Weights are calculated for every fifth day of the NSCAT period to reduce computer time. The timeseries of the weights shows no trend or pattern (Fig. 4). Therefore, an average value for each weight ($\beta_a = 3.12\times10^{-3}, \beta_b = 3.11\times10^{-3}$) is selected. The selected weights are used in the direct minimization to generate the daily pseudostress fields.

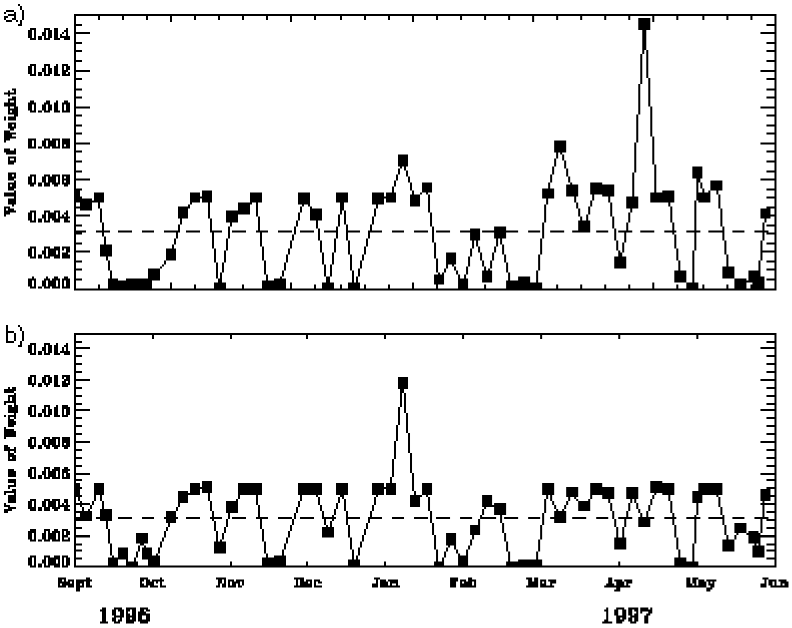

FIG. 4. Time series of the weights for the smoothing of the pseudostress (a), and smoothing of the curl of the pseudostress (b) constraints determined by cross validation. Weights are valid for the entire Pacific Ocean study region and are calculated roughly every five days (indicated by squares). No pattern or trend is apparent, and the average values (dashed lines) are used for the entire NSCAT period.

The impact of the difference between average weights and determined weights on the pseudostress fields is examined. Case I compares the pseudostress field for a day when the optimal weights are high (β_a = 7.02×10^{-3}, β_b = 1.12×10^{-2}) to the output from the average weights. Case II compares the pseudostress field for a day when the calculated weights are low ($\beta_a = 2.8 \times 10^{-4}$, $\beta_b = 2.5 \times 10^{-4}$) to the output from the average weights. Both cases show little sensitivity of the output field to the changes in weights. The RMS pseudostress component difference (followed by wind component differences in brackets) for case I are 2.45 m^2s^{-2} (0.16 ms^{-1}) for the *u* component and 2.08 m^2s^{-2} (0.15 ms^{-1}) for the *v* component. Case II has RMS differences of 6.19 m^2s^{-2} (0.55 ms^{-1}) and 5.90 m^2s^{-2} (0.56 ms^{-1}) for the *u* and *v* components respectively. The resulting output fields for cases I and II show little vector difference from the output field produced by using the average weights, which suggests that the average weights can be used to generate the pseudostress fields through direct-minimization for the entire NSCAT period.

Another consideration in sensitivity of the fields to errors in the weights is the impact of swath edge effects. The fields for which relatively small weights are found, are those that are relatively smooth or evolve very slowly in time. These fields show very little impact due to swath edge effects. The impact of using weights that are too large for these fields is very small. Conversely, those for which relatively large weights are found often have feature that move or evolve rapidly in time (e.g., translating cyclones or waves around Antarctica), and the swath edge effects are very important near these features. Consequently, the impact of using weights that are much too small is substantial. This is a very important consideration for oceanographic applications where erroneous curl and divergence of the forcing field has a large impact on model results. Therefore, erring by applying larger weights (but not too large) leads to less severe impacts in the fields.

3) Comparison to subjectively determined weights

Weights determined solely by visual inspection of a wind field results in subjective estimates of the weights ranging over ~4 orders of magnitude. The objectively determined weights fall within the range of subjectively determined weights; however, the range of ±20% for the objective technique is much smaller than for subjectively determined weights. The examples given above clearly show that the impact of a 20% error in weights is negligible in comparison to the uncertainty in NSCAT observations. Much larger errors in subjective estimates are not easily visible in plotted wind fields; however, they are apparent in derivatives of these fields. The objective technique combines these considerations to reduce the range of acceptable weights.

4) Spectra analysis

Energy density spectra (Fig. 5) can demonstrate the effectiveness of swath-edge removal and data filling, and the spectral slope can be compared to previous studies with other scatterometers. Energy density spectra are calculated for four latitudes (10°S, 10°N, 30°N, and 60°N), and averaged over 45 days from Jan. 17 through March 3, 1997. There are no substantial spikes in these spectra for the wavelengths expected to be associated with the sampling geometry (e.g., 400, 600, 1000, and 1600 km). The anomalies in the spectra for 10°S are likely due to the shorter distance over which the spectra are calculated. The distribution and width of gaps in daily coverage (Fig. 1) are functions of latitude, resulting in additional suspect wavelengths that vary as a function of latitude. The lack of such features is partial validation of the effectiveness of this gridding technique in handling edge effects and gaps in the observation.

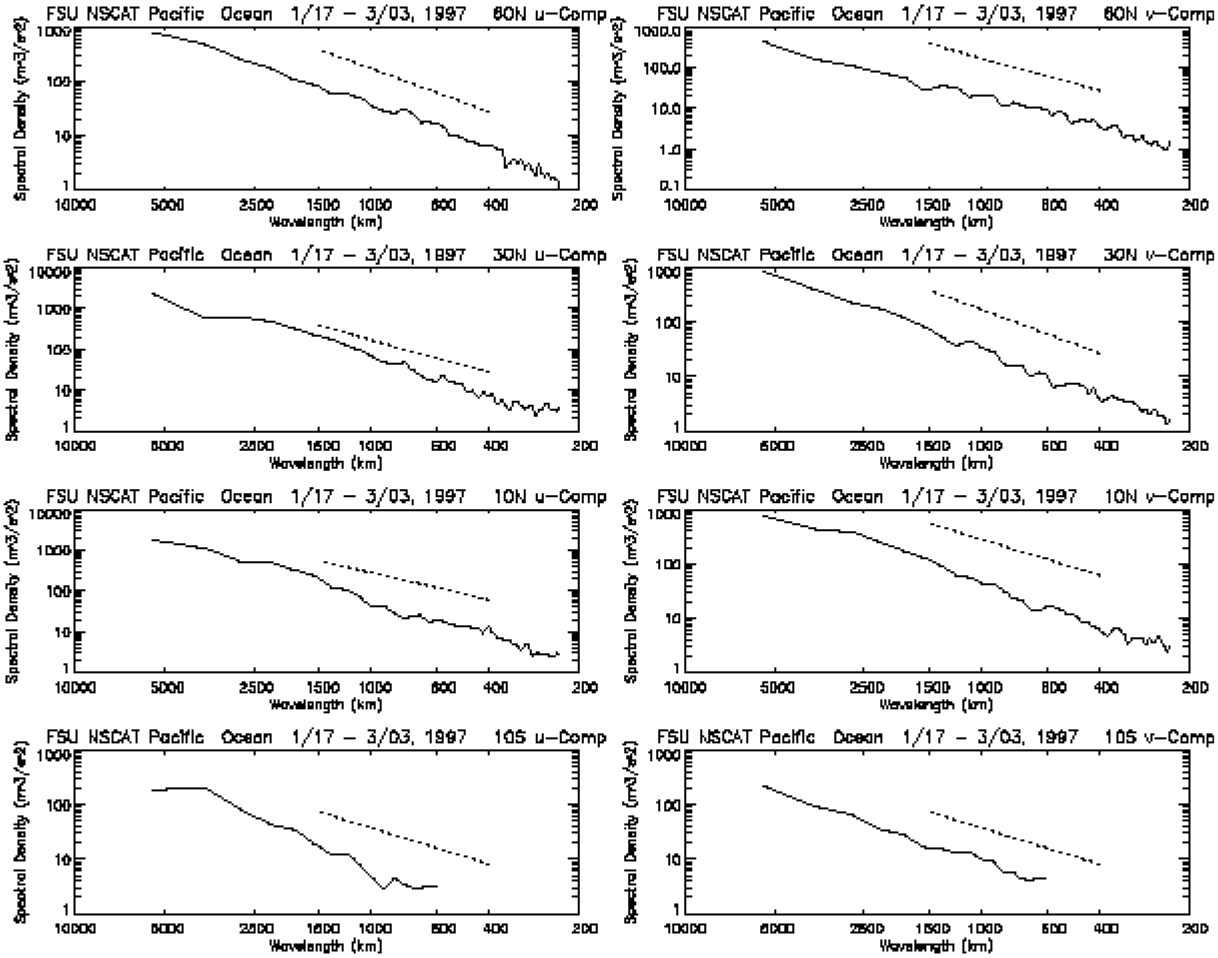

FIG. 5. Mean energy density spectra at four latitudes, averaged from Jan. 17, 1997 to March 3, 1997. The slope of the calculated spectra (solid lines) is similar to the slope found in previous studies of scatterometer winds (dashed lines).

Previous studies of wind component energy spectra (Freilich and Chelton 1986; Milliff et al., 1999b; Wikle et al., 1999) have found spectral slopes of approximately -5/3 in the tropics or approximately -2 in mid-latitudes. That is, $S \propto k^{-2}$, where S is the spectral density, and k is the wave number. The dashed lines in Fig. 5 for 10°S and 10°N have spectral slopes of -5/3, and of -2 for 30°N and 60°N. The spectral slopes determined from this gridded product are clearly similar to these obtained from previous studies, further validating this product.

b. Analysis of equatorial cold tongue region

The two average weights are applied to the direct minimization cost function and daily, 1°×1° pseudostress fields are constructed. These daily fields are publicly available (at http://www.coaps.fsu.edu/scatterometery/). They cover the Pacific Ocean between 40°S and 60°N for the entire NSCAT period**.**

The equatorial cold tongue region defined in the study as 15°S–15°N, 90°W–180° is examined closely. This region is looked into because it is a data sparse region for in-situ observations. Moving wind vector animations (Bourassa et al. 1998) show a high amount of variability in the ITCZ and the South Pacific convergence zone. Also, an anomalous westerly wind associated with the onset of El Niño creates vortices just north and south of the equator that are short lived. This high amount of detail is not attainable from in-situ data.

This region is further studied through a CEOF analysis (Horel 1984; Putman et al. 2000) of the daily pseudostress fields. Briefly, a CEOF analysis is a EOF analysis that can be applied to vectors: it calculates eigenvalues and eigenvectors from a covariance matrix. The equation

$$\mathbf{S}_N = \sum_{n=1}^{nt} \left[\mathbf{u}(n) \mathbf{E}_N^*(n) \right] \tag{7}$$

calculates the N^{th} spatial function ($\mathbf{S}_N$) from the data, where nt is the length of the time record, $\mathbf{u}$ is the pseudostress field, and $\mathbf{E}^*$ is the complex conjugate eigenvector. The temporal mean zonal and meridional pseudostresses (Fig. 6) are removed prior to the analysis. The CEOF results in 276 spatial functions and eigenvectors (principal components). Each principal component represents a certain percentage of the variance (in both space and time) given by the eigenvalues. The eigenvector (time series) has both an amplitude and rotation angle. The amplitude multiplied by the spatial function gives the spatio-temporal variability of the principal component, and the rotation angle represents the counterclockwise rotation of each vector in the spatial function. The original data set can be reproduced by calculating the sum of the product of every eigenvector and spatial function.

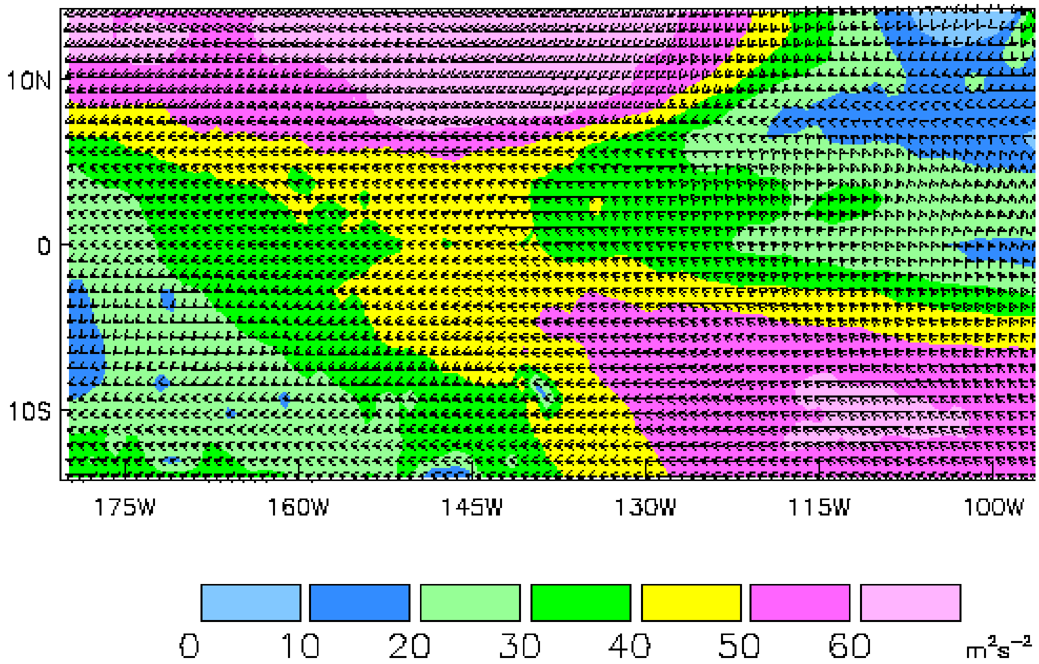

FIG. 6. Mean pseudostress of the equatorial cold tongue region for the NSCAT period from the objectively derived NSCAT pseudostress fields. This mean is removed prior to the CEOF analysis. The Northeast and Southeast trade winds are apparent, as well as the gap flow through the Sierra Madres (upper right hand corner).

A scree test (Wilks 1995) is used to determine which principal components are statistically significant. The first four modes, which contain 43% of the variance, are statistically significant (Fig. 7).

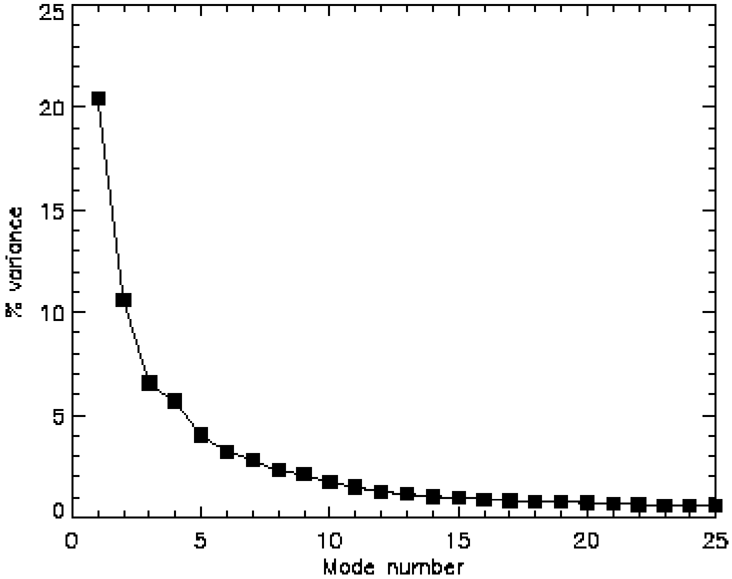

FIG. 7. A Scree diagram showing the percent variance associated with the first 25 modes of the CEOF analysis. The first four modes are statistically significant.

1) Principal component 1

The first mode (Fig. 8) represents 20.44% of the variance. The principal component has most of the variance associated with the changes in Northern Hemisphere trade winds and a lesser amount with the Southern Hemisphere trade winds in the western Pacific. A rotation of the spatial function by 180° increases the Northern Hemisphere trades and decreases the Southern Hemisphere trades.

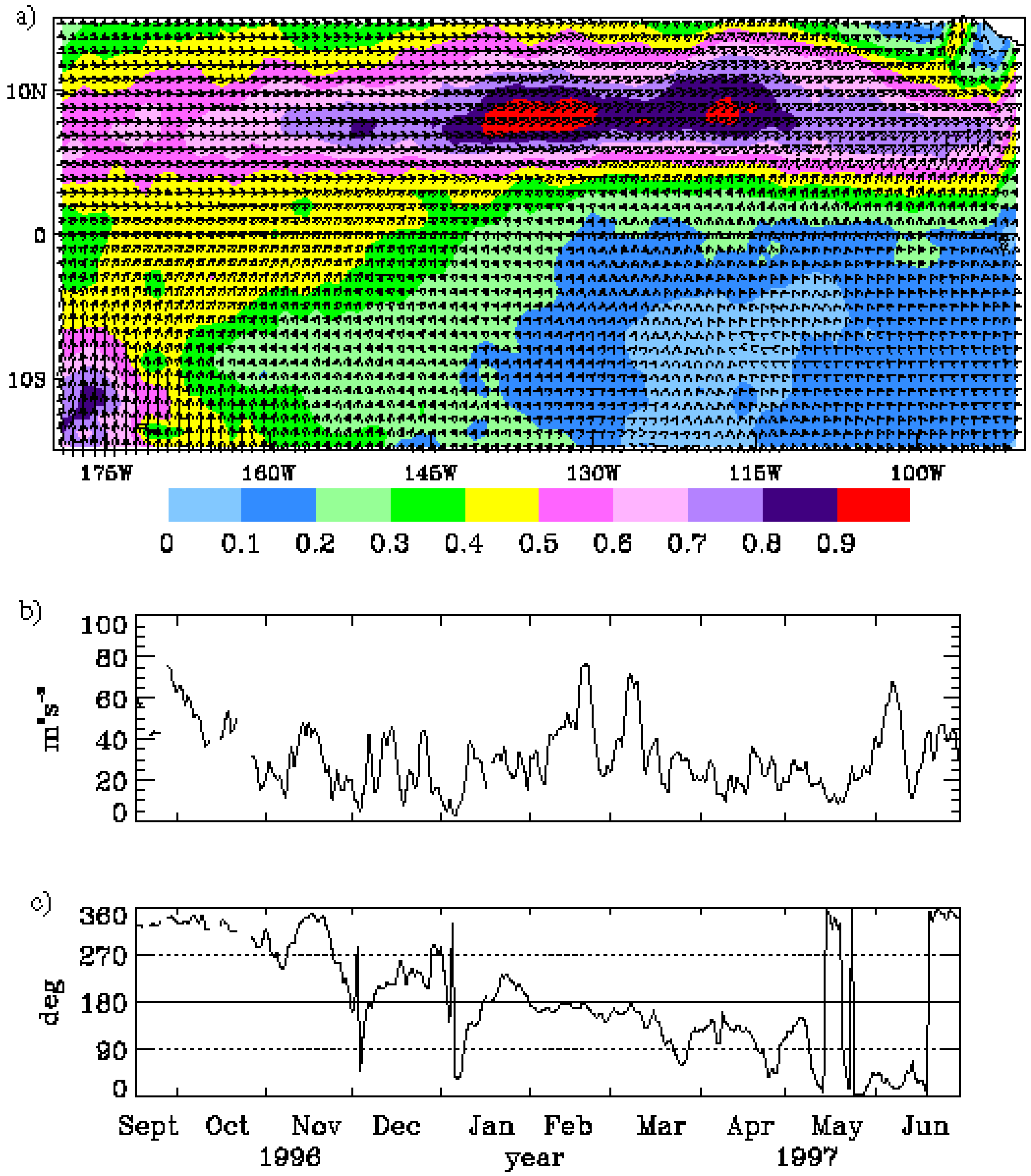

FIG. 8. Principal Component 1 contains 20.44% of the variance. The spatial function (a) multiplied by the amplitude of the eigenvector (b) gives the magnitude of the pseudostress. Rotation angle (c) is a counterclockwise rotation of the spatial function vectors. Gaps in the time series indicate days that were excluded from the CEOF analysis due to missing data.

The time series of the rotation angle (Fig. 8c) shows the seasonal change in the strength of the tradewinds. The amplitude (Fig. 8b) also has a strong seasonal signal, with maxima in the winter and summer and minima in the fall and spring which is expected for equatorial winds, and supported by the FSU winds climatology (Stricherz et al. 1997). Spectral analysis of the amplitude (Fig. 9a) shows energy in periods greater than 50 days and at time scales near 20 days. A rotary spectrum (Fig. 10a; O'Brien and Pillsbury 1974) shows a clockwise rotation of the trade winds (negative period) on an annual time scale. This result shows that the massive El Niño beginning near the end of this study period had little impact on this mode for this region and time.

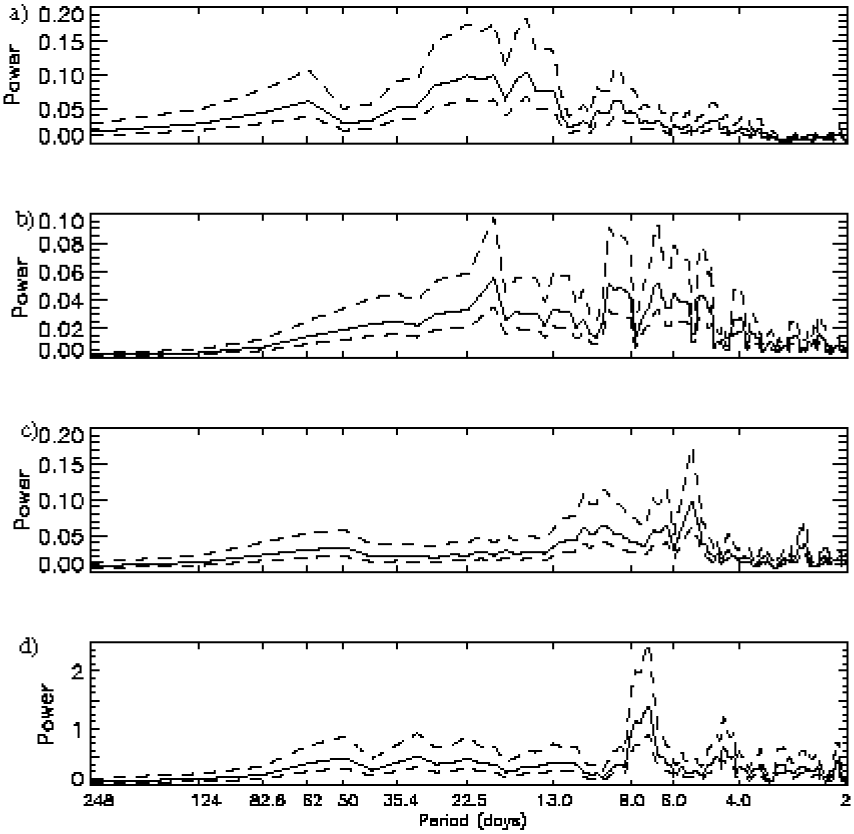

FIG. 9. Spectral analysis of the eigenvector amplitude for principal components 1 (a), 2 (b), 3 (c) and 4 (d). Power is plotted against period in days (in an area preserving plot). Confidence limits

(90%) are shown as the dashed lines. The spectrum is smoothed using a five point running mean. The time period analyzed is Oct. 25, 1996 – June 29, 1997. Data before Oct. 25 had numerous missing days and are omitted from the spectral analysis. One other missing day (Jan. 16) in the time series is linearly interpolated.

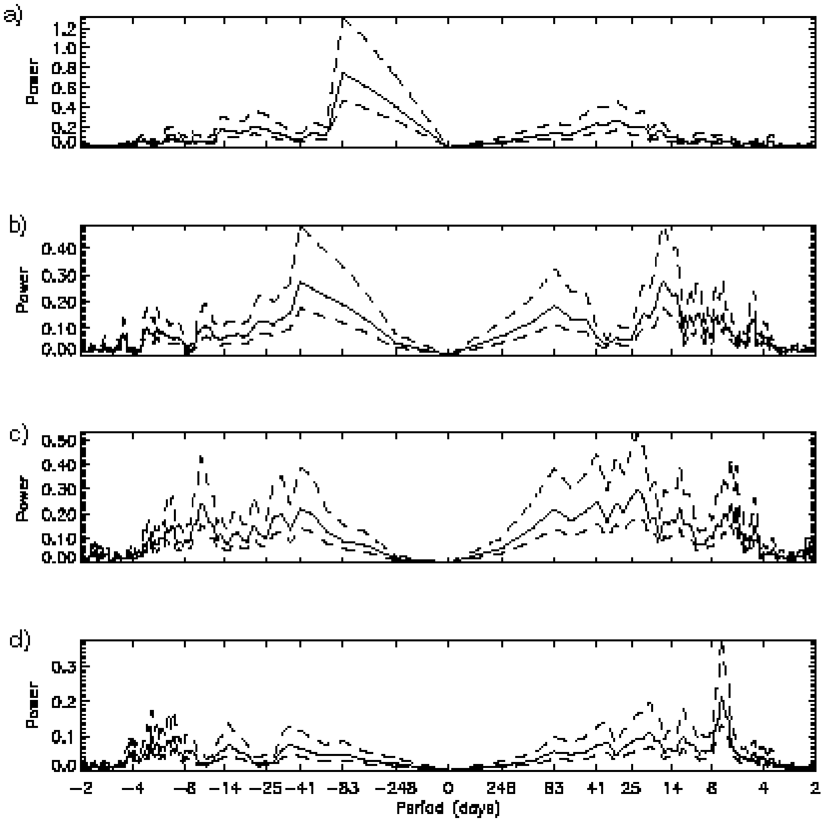

FIG. 10. Rotary spectra for the complex eigenvectors of principal components 1 (a), 2 (b), 3 (c) and 4 (d). Power is plotted against rotation period in days (in an area preserving plot). Confidence intervals (90%) are shown as dashed lines. Positive (negative) periods indicate counterclockwise (clockwise) rotation.

2) Principal component 2

The second mode (Fig. 11) represents 10.63% of the variance. This mode's variance is associated with the western portion of the northeast and southeast trades. In the fall, the spatial function is rotated by 90° and anomalous convergence occurs along the equator. The spring has a rotation angle around 270°, with anomalous divergence occurring along the equator. The winter months are a transition time, when the angle rotates from 90° through 180° to near 270°.

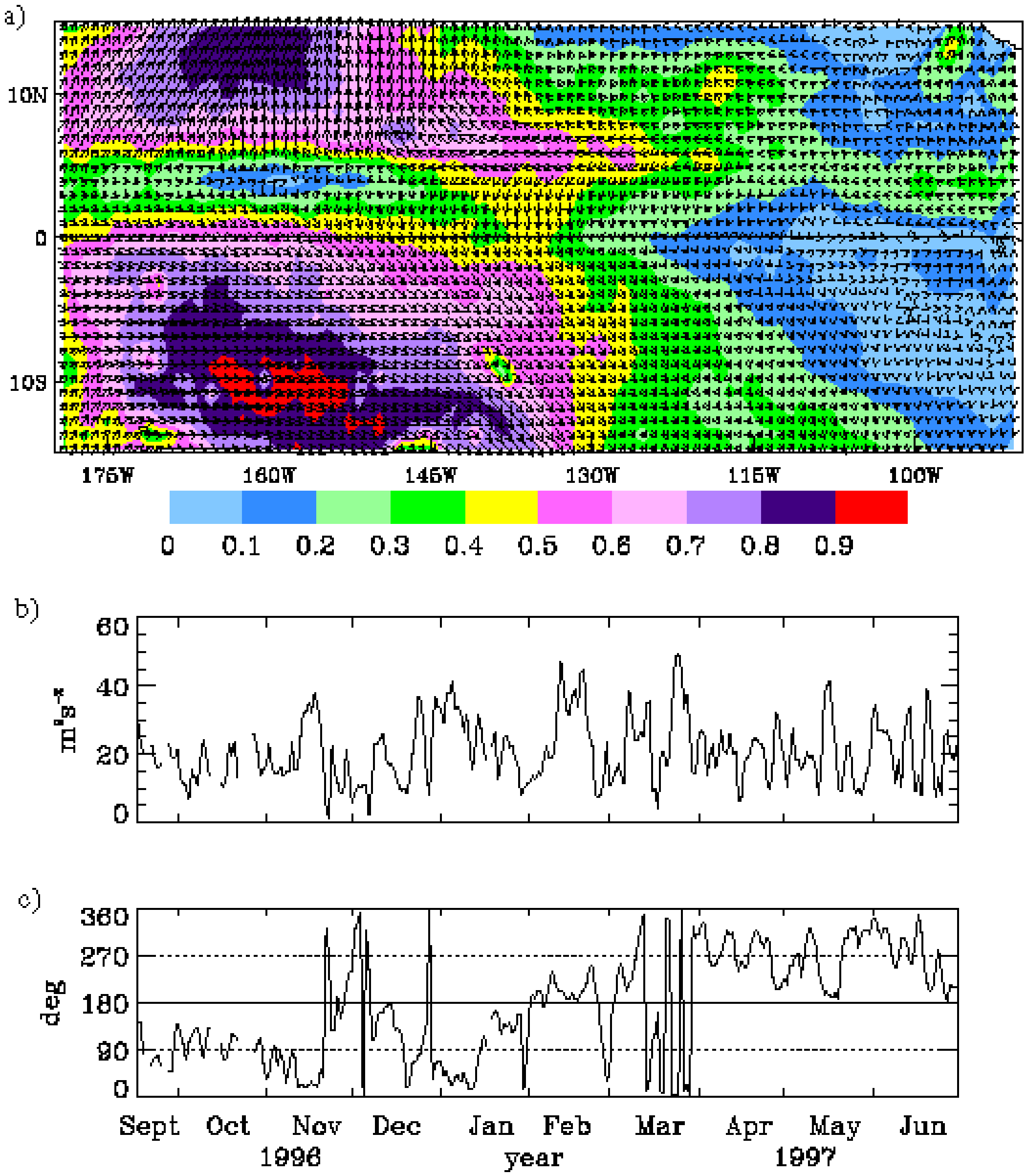

FIG. 11. As for Fig. 8, except for the second principal component has of 10.63% of the variance.

A spectral analysis of the time series of the amplitude (Fig. 9b) shows a signal at a period 20.6 days, and a synoptic signal. Tropical Ocean-Atmosphere (TAO) buoy observations for the same time period at 8°S and 170°W also show a period near 20 days in the magnitude of the pseudostress (Fig. 12a). The rotary spectrum of the complex eigenvector (Fig. 10b) shows a counterclockwise rotation with a period between 40 and 80 days, and a counterclockwise rotation of 80 days and about 14 days. The rotary spectrum of the TAO buoy (Fig. 12b) has similar results. Supporting the conclusion that the 20 day signal is geophysical in origin, rather than an artifact of the orbital pattern of the satellite.

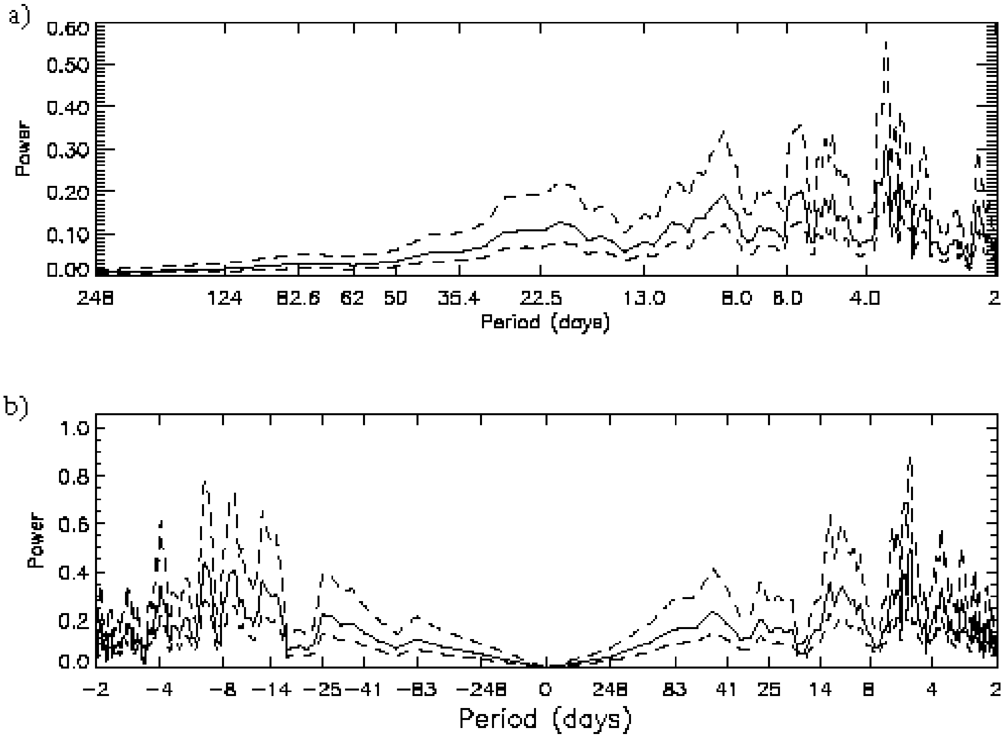

FIG. 12. Spectral analysis of TAO buoy data located at 8°S, 170°W. Pseudostress magnitude (a), and rotary wind spectra (b). Power is plotted against period in days, and is smoothed using a five point running mean. Time period analyzed is the same as Fig. 9 (10/25/96 – 6/29/97), with missing days linearly interpolated. A period of near 20 days (a) matches the result of the spectral analysis of the second principal component's eigenvector (Fig. 9b), and a

counterclockwise rotation (positive period) of near 80 days (b) matches the second principal component’s rotary spectrum (Fig. 10b).

Waves in the SST field for the tropical eastern Pacific with 20–30 day periods were found by Legeckis (1977) and Philander et al. (1985). Also, a mixed Rossby–gravity wave with a period of 20 days that caused an oscillation in the meridional current was noted by Halpern et al. (1988). These oscillations may be related to the 20-day period in the eigenvector amplitude.

3) Principal component 3

The third mode (Fig. 13) represents 6.56% of the variance. The variance is associated with the South Pacific convergence zone, and the extreme western and eastern portions of the northeast trades. Late November, early December, early February, and the middle of May through the end of the NSCAT period have a rotation angle of 0°. This rotation angle indicates anomalous convergence from 0°, 180° to 10°S, 160°W and anomalous convergence from 10° to 15°N, and from 140° to 110°W. March and April have the spatial function rotated by 180°. This springtime pattern has anomalous divergence in the southwestern portion of the equatorial cold tongue region and divergence north of the equator. Anomalous convergence in the area of the SPCZ is strongest in the fall, early winter, and June. There is anomalous divergence in this area in the late winter and spring.

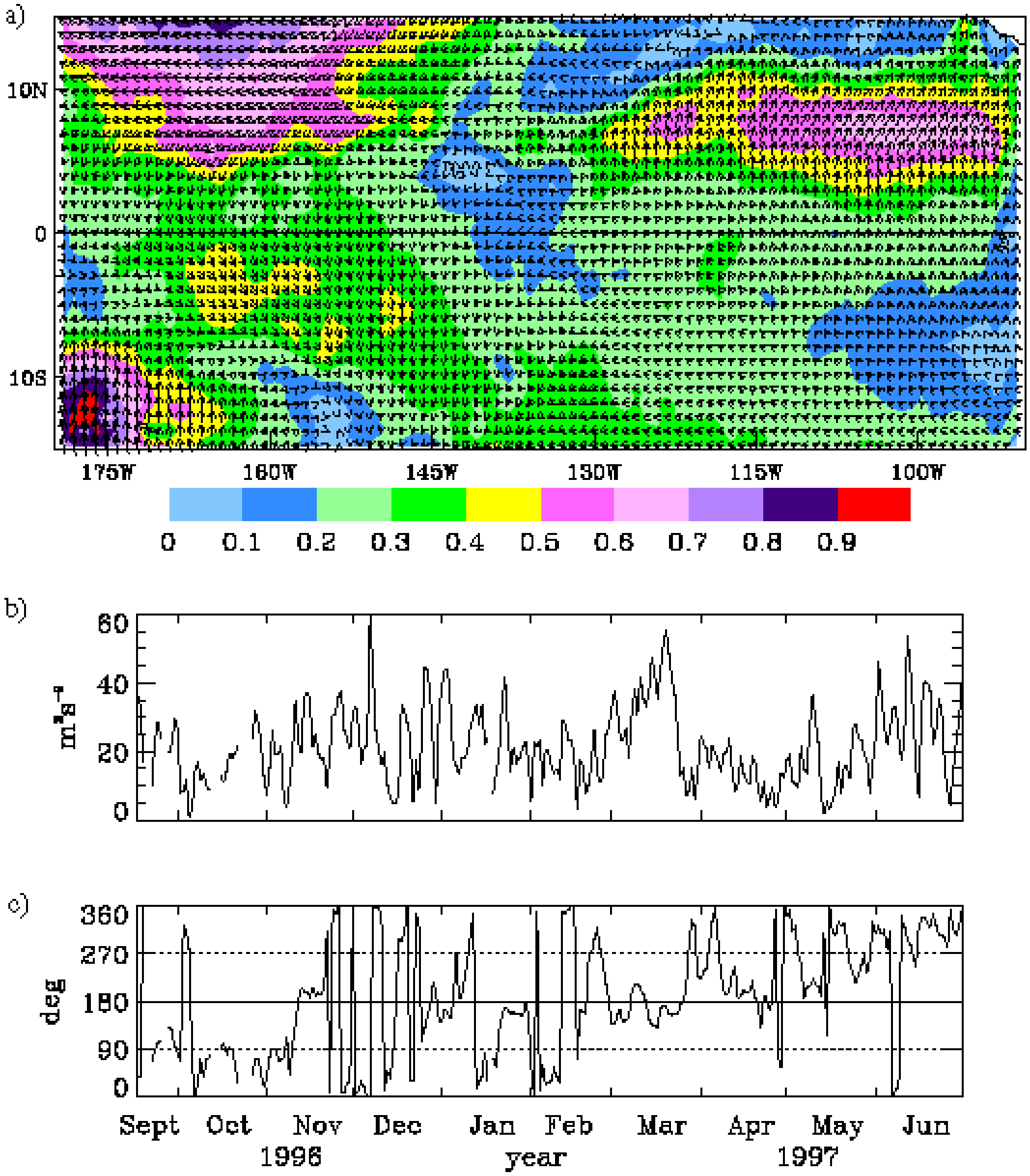

FIG. 13. As for Fig. 6, except for the third principal component which has 6.56% of the variance.

The time series of the amplitude vector show three peaks, one in early December (rotation of 0°), one in mid March (rotation of 180°), and the last in early June (rotation near 0°). A spectral analysis of the amplitude time series (Fig. 9c) shows a signal at a period of 50 days. The 50 day period may be associated with the Madden–Julian oscillation (Madden and Julian 1971; Lau and Chan 1988).

4) Principal component 4

The fourth mode (Fig. 14) represents 5.69% of the variance. A large portion of the variance in this mode is associated with the eastern portion of the northeasterly trades, the gap flow through the Sierra Madres (Bourassa et al. 1999), and the central portion of the southeast trades. With a rotation of 0°, the spatial function has an anomalous convergence zone running from 150° to 110°W centered near 8°N. A rotation angle between 90° and 200° of the spatial function results in an anomalous divergent zone for this area. The peak of the amplitude (Fig. 14b) in December is associated with strong convergence at 8°N and divergence along the equator. The peaks in March and June are associated with divergence in the area of the ITCZ (Rasmusson and Carpenter 1982) and convergence on the equator.

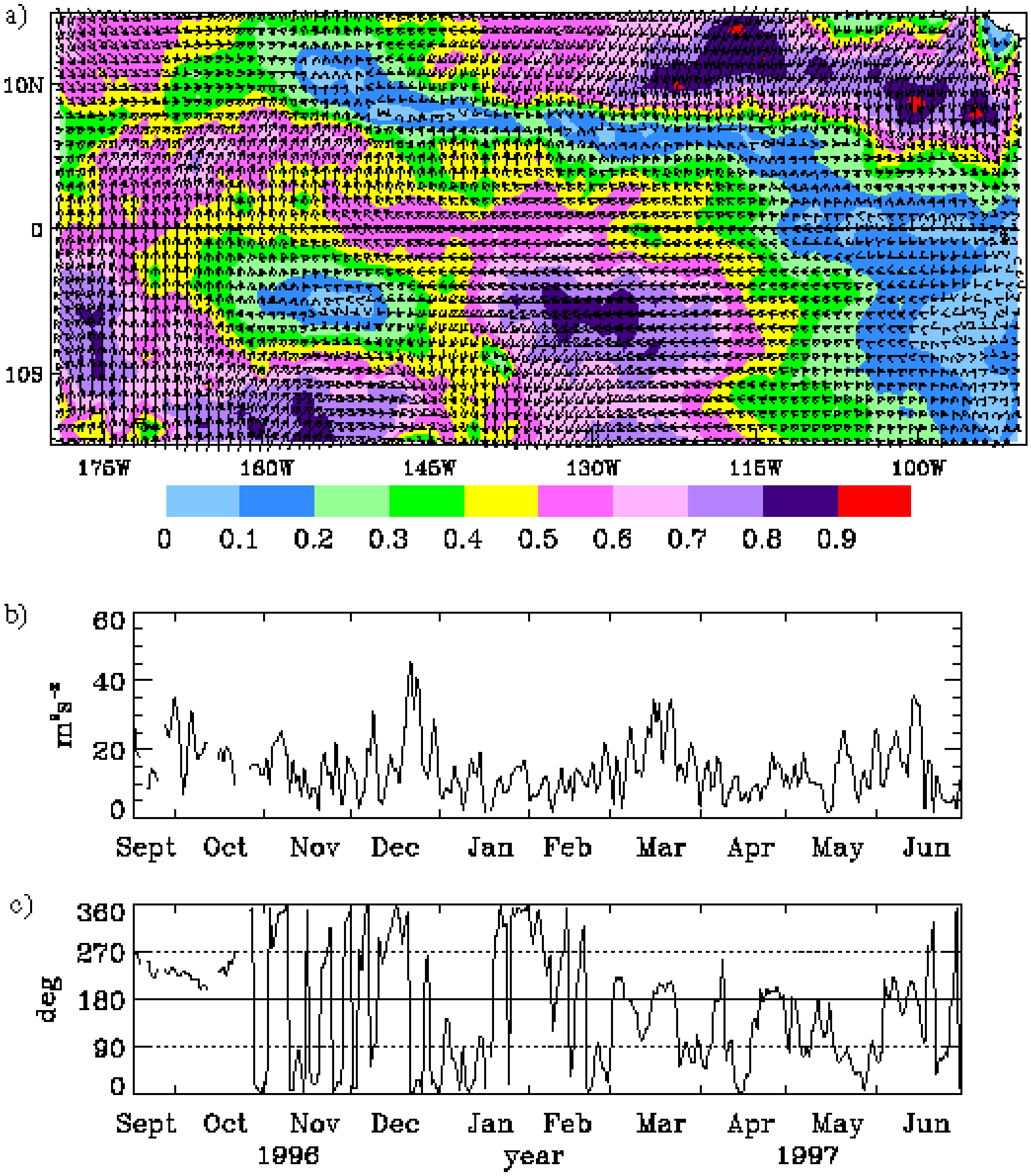

FIG. 14. As for Fig. 6, except for the fourth principal component, which has 5.69% of the variance.

Spectral analysis of the magnitude shows variability on the order of 50, 30, and near 7 days. TAO buoy data from 5°S and 135°W show a similar signal between 30–50 days and at 7 days for the NSCAT period (Fig. 15a). Rotary spectral analysis (Fig. 10d) shows counterclockwise rotations between 40 and 80 days that correspond to the TAO buoy data (Fig. 15b). The TAO buoys confirm that for this study the periodic changes in pseudostress are not a satellite sampling problem, but that they occur in nature.

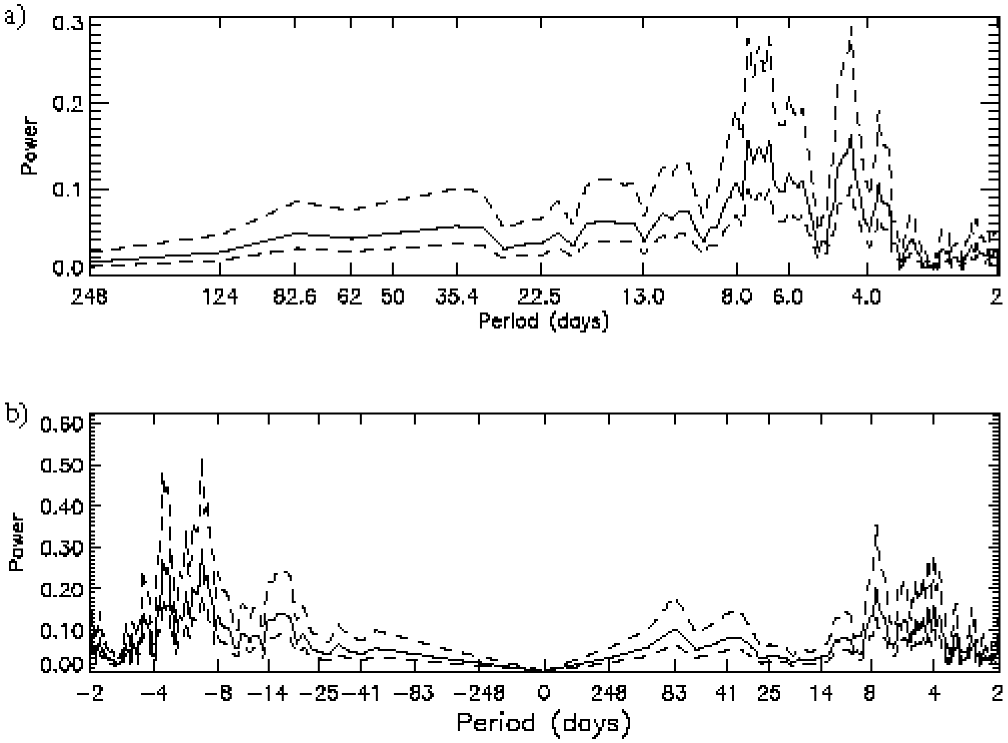

FIG. 15. Same as Fig. 9, except the TAO buoy was located at 5°S, 125°W. Magnitude of pseudostress (a) shows a period near 7 days and a period between 30 and 50 days that are similar to the periods of the fourth principal component's eigenvector (Fig. 9d). Rotary wind spectrum (b) shows an annual signal and a signal near 40 to 80 days with counterclockwise rotations, which is also found in the fourth principal component's rotary spectrum (Fig. 10d).

c. Comparison to FSU winds

Monthly means of the objectively derived NSCAT pseudostresses are validated with the FSU winds (Stricherz et al. 1997), which use in-situ data to derive monthly pseudostress fields for the equatorial Pacific Ocean. NSCAT wind and pseudostress vectors are calibrated to a height of 10 m. Pseudostresses can be height adjusted, assuming neutral stability, using a log wind profile, to the 20 m height of the FSU winds. This doubling of height results in a ~13% increase of NSCAT pseudostresses. When this adjustment is made, the two data sets show many of the same large-scale features that are similar in magnitude. The NSCAT pseudostress has greater spatial detail, such as the gap flow through the Sierra Madres (Fig. 16), and tropical cyclones in the western Pacific, which are not in the FSU wind analysis (Fig. 17).

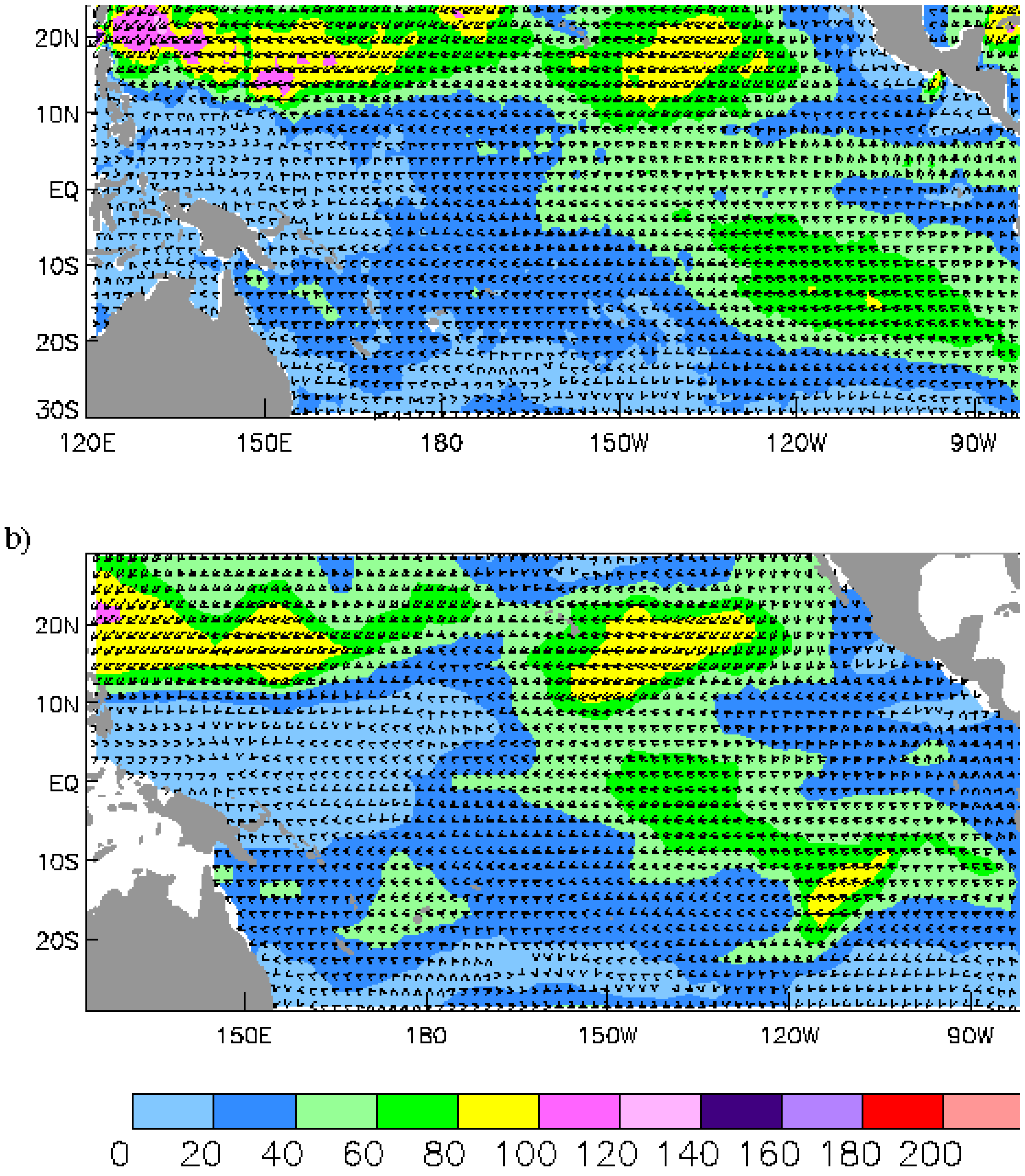

FIG. 16. November 1996 mean pseudostress for the objectively derived NSCAT fields (1° by 1° resolution) adjusted to a height of 20 m (a), vectors are plotted every 2° by 2° for clarity. FSU winds monthly pseudostress (2° by 2° resolution) valid for the same time (b). Magnitude of the pseudostress is contoured and direction is indicated by vectors. Magnitudes of the two products are similar but the NSCAT product has finer detail such as the flow off of Central America and the cross equatorial flow in the eastern Pacific.

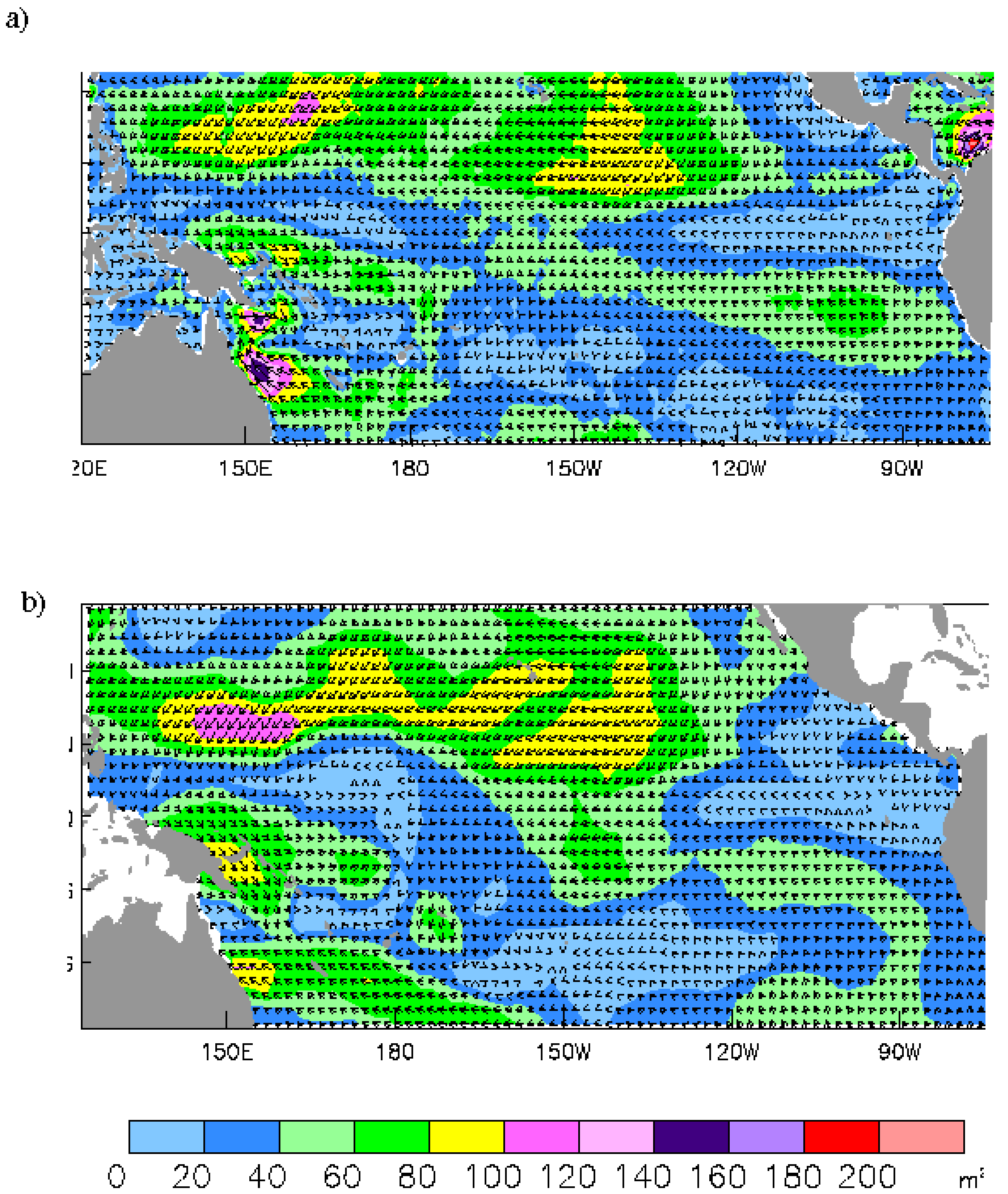

FIG. 17. Same as Fig. 16 except for May 1997. NSCAT product (a) shows high values of pseudostress off of the coast of Australia which are missing in the FSU wind analysis (b).

d. Comparison to NCEP reanalysis

The NSCAT-derived pseudostresses are converted to wind vectors and compared to the NCEP reanalysis. Wind patterns and magnitudes (Fig. 18) are generally similar in both products. The tropical eastern Pacific is one area where there is a substantial difference between the two products. In this area, the NSCAT-derived field has stronger trade winds. The eastern Pacific is a region where NCEP is known to underestimate the trade winds (Putman et al. 2000). Another difference is the amount of detail resolved by the two products. The NCEP reanalysis product is on a Gaussian grid (approximately 2° by 2°), while the NSCAT derived fields are gridded on 1° by 1°. The smoother appearance of the NCEP vorticity field (Fig. 18) is due to this coarser grid and lack of impact of surface wind observations. The NCEP reanalysis did not assimilate NSCAT data, and in-situ surface wind observations from TAO buoys and volunteer observing ships (VOS) are poorly assimilated. Therefore the NCEP background field, generated from a 6 hour forecast, is only slightly modified by observations in this region.

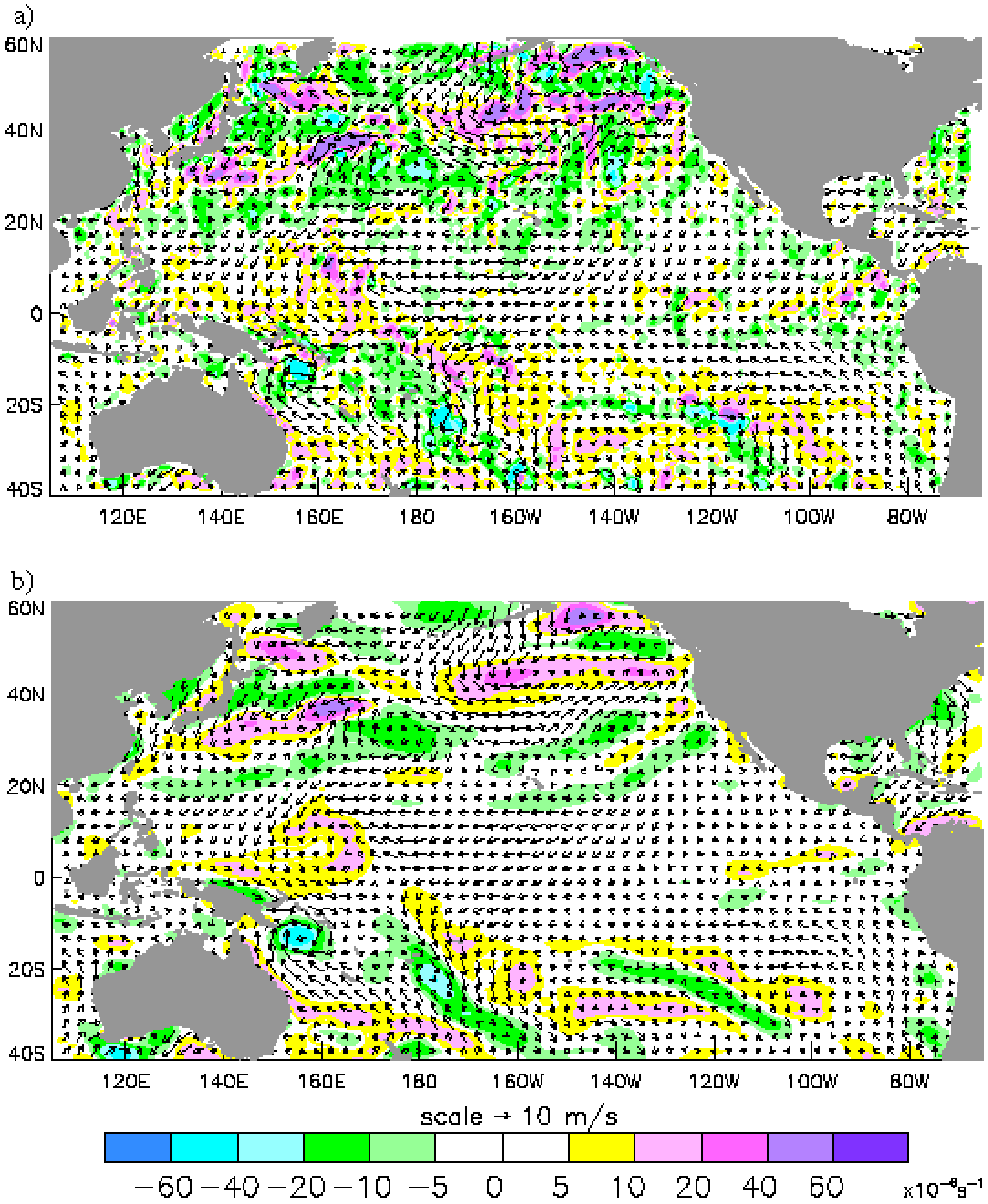

FIG. 18. Objectively derived NSCAT winds (a) and NCEP reanalysis (b) for March 16, 1997. Wind component are interpolated to a 1° by 1° grid and vorticity is contoured. Wind vectors are plotted on a 3° by 3° grid for clarity. The NSCAT product has stronger trade winds and stronger winds off of the coast of Central America. NSCAT also shows more detail of storms than NCEP.

The average specific kinetic energy of the NSCAT derived field is compared to NCEP and to NSCAT observations (Table 3). NCEP has average specific kinetic energy that is lower (~12%) than the NSCAT derived field, which is slightly lower (~1.5%) than that of the NSCAT observations. A source for the difference in the kinetic energy is the weaker trade winds analyzed by NCEP. Furthermore, the higher kinetic energy in the derived NSCAT fields are supported by the kinetic energy in the NSCAT observations.

5. Conclusions

An objective technique is used to produce daily pseudostress fields based purely on NSCAT observations. Three weighted constraints specify the conditions for which the pseudostress fields are optimized. The constraints are a misfit to observations, a Laplacian smoothing, and a kinematic constraint (the curl of the pseudostress). These weights are objectively determined through cross validation, which is a computationally expensive technique. The number of computations is further increased by the large size of the study region, 14,321 ocean grid points. A reduction in the number of calculations is necessary for practical application of cross validation. This reduction is achieved through the technique of multigridding (i.e., initially performing calculations on a coarser grid). The near independence of the weights on spatial grid resolution (up to at least 6°) demonstrates the validity of multigridding applied to cross validation.

This new gridded product is an improvement on the temporally-weighted winds and other gridded NSCAT products due to the reduction of temporal smoothing and better removal of the satellite tracks from the curl field. These daily fields have kinetic energy similar to the NSCAT observations and NCEP reanalysis daily winds for the mid-latitudes. The daily gridded NSCAT winds have much stronger trade winds than are found in the NCEP reanalysis, where the winds are known to be weak. Monthly averages of these winds have patterns that are similar to FSU winds. After a height adjustment (from 10 to 20 m) the objective product also has magnitudes similar to FSU winds.

The high spatial and temporal grid resolution of the daily pseudostress fields allows for detailed analyses of wind patterns in sparsely observed regions. A CEOF analysis of the equatorial cold tongue region shows that there is a strong seasonal component to the trade winds in the first principal component. In the second principal component, there is a 20 day oscillation in the magnitude of the pseudostress, which is also found in TAO buoy wind observations. This periodicity could be associated with a mixed Rossby–gravity wave in the area. The third principal component shows fluctuations in the magnitude of the pseudostress related to the South Pacific convergence zone. Synoptic variability associated with the gap flow through the Sierra Madres is evident in the fourth principal component.

The objective techniques of direct-minimization and cross validation can be applied to any set of observations that have incomplete spatial coverage. The SeaWinds scatterometer recently launched on the QuikScat satellite will provide a new generation of scatterometer data to which this technique can be applied. The utilization of cross validation to determine the weights removes the subjective judgement of the researcher and allows for the proper amount of information from the observations to go into the final product.

Acknowledgments: We thank Bob Atlas, Ross Hoffman, and Ralph Milliff for their discussions. Funding for this project is from the NASA JPL NSCAT and NASA OSU SeaWinds

projects. COAPS received its base funding from the ONR’s Secretary of Navy Grant to James J. O’Brien.

REFERENCES

Atlas, R., R. N. Hoffman, S. C. Bloom, J. C. Jusem, and J. Ardizzone, 1996: A multiyear global surface wind velocity dataset using SSM/I wind observations. *Bull Amer. Metoer. Soc.*, **77**, 869-882.

Atlas, R., S. C. Bloom, R. N. Hoffman, E. Brin, J. Ardizzone, J. Terry, T. D. Bungato, and J. C. Jusem, 1999: Geophysical validation of NSCAT winds using atmospheric data and analyses. *J. Geophys. Res.,* **104**, 11,405-11,424.

Bentamy, A., B., H. Grima, and Y. Quilfen, 1998: Validation of the gridded weekly and monthly wind fields calculated from ERS-1 scatterometer wind observations. *Global Atmos. Ocean Syst.*, **6**, 373-396.

Bentamy, A., Y. Quilfen, F. Gohin, N. Grima, M. Lenaour, and J. Servain, 1996: Determination and validation of average wind fields from ERS-1 scatterometer measurements. *Global Atmos. Ocean Syst.,* **4,** 1-29.

Bourassa, M. A., M. H. Freilich, D. M. Legler, W. T. Liu, and J. J. O’Brien, 1997: Wind observation from new satellite and research vessels agree. *Eos Trans. Amer. Geophys. Union,* **78**, 597-602.

Bourassa, M. A., D. M. Legler, J. J. O’Brien, J. N. Stricherz, and J. Whalley, 1998: High temporal and spatial resolution animations of winds observed with the NASA scatterometer, *14th Int. conf. on Interactive Information Processing Systems*, January, Phoenix, AZ, Amer. Meteor. Soc., 556–559.

Bourassa, M. A., L. Zamudio, and J. J. O'Brien, 1999: Noninertial flow in NSCAT observations of Tehuantepec winds. *J. Geophys. Res.,* **104**, 11,311-11,320.

Brandt, A. 1982: Guide to multigrid development. *Proceedings of a conference (Köln- Porz, November 1981)*, [Available from the Department of Applied Mathematics, Multigrid Methods, eds. W. Hackbusch and U Trottenberg, Springer-Verlag, pp.220-312.

Brandt, A., 1982: Guide to multigrid development, in MULTIGRID METHODS, Hackbusch, W. and Trottenberg, U., eds., Springer-Verlag, pp. 220-312.

Caruso, M. J., S. Dickinson, K. A. Kelly, M. Spillane, L. J. Mangum, M. McPhaden, and L. D. Stratton, 1999: Evaluation of scatterometer winds using Equatorial Pacific buoy observations. WHOI-99-10, 62 pp., Available from Woods Hole Oceanographic Institution, Woods Hole, MA, 02543.

Chelton, D. B., and F. J. Wentz, 1986: Further development of an improved altimeter wind speed algorithm, *J. Geophys. Res.,* **91**, 14250-14260.

Chelton, D. B., M. H. Freilich, and S. K. Esbensen, 2000a: Satellite observations of the wind jets off the Pacific coast of Central America, Part I: Case studies and statistical characteristics. *Mon. Wea. Rev*., **128**, in press.

Chelton, D. B., M. H. Freilich, and S. K. Esbensen, 2000b: Satellite observations of the wind jets off the Pacific Coast of Central America, Part II: Regional relationships and dynamical considerations. *Mon. Wea. Rev*., **128**, in press.

Chen, D., M. A. Cane, and S. E. Zebiak, 1999: The impact of NSCAT winds on prediction the 1997/1998 El Nino: A case study with the Lamon-Doherty Earth Observation model. *J. Geophys. Res.*, **104**, 11,321-11,328.

Chin, T. M., R. F. Milliff, and W. G. Large, 1998: Basin scale, high-wavenumber sea surface wind fields from a multiresolution analysis of scatterometer data. *J. Atmos. Oceanic. Technol.*, **15**, 741-763.

Elsner, J. B., and C. P. Schmertmann, 1994: Assessing forecast skill through cross validation. *Wea. Forecasting.*, **9**, 619-624.

Freilich, M. H., and R. S. Dunbar, 1999: The accuracy of the NSCAT 1 vector winds: comparisons with National Data Buoy Center buoys. *J. Geophys. Res*., **104**, 11,231-11,246.

Gonzales, A. E. and D. G. Long, 1999: An assessment of NSCAT ambiguity removal*. J. Geophys. Res.*, **104**, 11449-11458.

Graber, H. C., A. Bentamy and N. Ebuchi, 1997: Evaluation of scatterometer winds with ocean buoy observations. *Proc. Scatterometer Symp.*, Maui, NASA, 152-153. [Available from Scatterometer Projects Office, Jet Propulsion Lab., Pasadena, CA 91109].

Halpern, D., R. A. Knox, and D. S. Luther, 1988: Observations of 20-day meridional current oscillations in the upper ocean along the Pacific equator. *J. Phys. Oceanogr.*, **18,** 1514-1534.

Horel, J. D., 1984: Complex principle component analysis: theory and examples, *J. Climate Appl. Meteor.*, **23**, 1660-1673.

Kalnay, E., M. Kanamitsu, R. Kistler, W. Collins, D. Deaven, L. Gandin, M. Iredell, S. Saha, G. White, J. Woolen, Y. Zhu, M. Chelliah, W. Ebisuzaki, W. Higgins, J. Janowiak,. K. C. Mo, C. Ropelewski, J. Wang, A. Leetma, R. Reynolds, R. Jenne, and D. Joseph, 1996: The NCEP/NCAR 40-year reanalysis project, *Bull. Amer. Meteor. Soc.*, **77**, 437-77,471.

Kelly, K. A., S. Dickinson, and Z.-J. Yu, 1999: NSCAT tropical wind stress maps: implications for improving ocean modeling. *J. Geophys. Res.*, **104**, 11,291-11,310.

Kutsuwada, K., 1998: Impact of wind/wind-stress field in the North Pacific constructed by ADEOS/NSCAT data. *J. Oceanogr.*, **54**, 443-456.

Lau, K. M., and P. H. Chan, 1988: Intraseasonal and interannual variations of tropical convection: a possible link between the 40-50 day oscillation and ENSO*? J. Atmos. Sci*., **45**, 506-521.

Legeckis, R. 1977: Long waves in the eastern equatorial Pacific Ocean: A view from a geostationary satellite. *Science,* **197**, 1179-1181.

Legler, D., and J. J. O'Brien, 1985: Development and testing of a simple assimilation technique to derive average wind fields from simulated scatterometer data, *Mon. Wea. Rev.*, **113**, 1791-1800.

Legler, D. M, I. M. Navon, and J.J. O’Brien, 1989: Objective analysis of pseudostress over the Indian Ocean using a direct-minimization approach. *Mon. Wea. Rev*., **117,** 709-720.

Legler, D. M., J. N. Stricherz, and J. J. O’Brien, 1997: TOGA pseudostress atlas 1985-1994: III Indian Ocean, *COAPS Rep.* 97-3, 175 p. [Available from COAPS, The Florida State University, Tallahassee, FL 32306].

Madden, R. A., and P. R. Julian, 1971: Detection of a 40-50 day oscillation in the zonal wind in the tropical Pacific. *J. Atmos. Sci.*, **28**, 702-708.

Meyers, S. D., C. S. Jones, D. M. Legler, and J. J. O’Brien, 1994: The sensitivity of parametric variations in direct minimization techniques. *Mon. Wea. Rev.*, **122**, 1632-1639.

Michaelsen, J., 1987: Cross validation in statistical climate forecast models. *J. Climate Appl. Meteor.*, **26**, 1589-1600.

Milliff, R. F.,T. J. Hoar, H. van Loon, and M. Raphael, 1999a: Quasi-stationary wave variability in NSCAT winds. *J. Geophys. Res.*, **104**, 11,425-11,426.

Milliff, R. F., W. G. Large, J. Morzel, G. Danabasoglu, and T. M. Chin, 1999b: Ocean general circulation model sensitivity to forcing from scatterometer winds. *J. Geophys. Res.*, **104**, 11,337-11,358.

Naderi, F. M., Freilich, M. H. and Long, D. G., 1991: Spaceborne radar measurements of wind velocity over the ocean- an overview of the NSCAT scatterometer system. *Proc. IEEE,* **79**, 850-866.

O'Brien, J. J., and R. D. Pillsbury, 1974: Rotary wind spectra in a sea breeze regime. *J. Appl. Meteor*., **13**, 820-825.

Polito, P. S., W. T. Liu and W. Tang, 1997: Correlation-based interpolation of NSCAT wind data. Proc. Scatterometer Symp., Maui, 30-32. [Available from Scatterometer Projects Office, Jet Propulsion Lab., Pasadena, CA 91109].

Philander, S. G. H., D. Halpern, R. Legeckis, L. Miller, C. Paul, R. Watts, R. Weisberg, and M. Wimbush, 1985: Long waves in the equatorial Pacific Ocean. *EOS Trans. Amer. Geophys. Union,* **66**, 154-156.

Pierson, W. J., Jr., 1990: Examples of, reasons for and consequences of poor quality of wind data for the marine boundary layer: implications for remote sensing. *J. Geophys. Res.*, **95**, 13313-13340.

Putman, W. M., D. M. Legler, and J. J. O'Brien, 2000: Interannual variability of synthesized FSU and NCEP reanalysis pseudostress products over the Pacific Ocean. *J. Climate*, in press.

Rasmusson, E. M. and T. H. Carpenter, 1982: Variations in tropical sea surface temperature and surface wind fields associated with the Southern Oscillation/ El Niño. *Mon. Wea. Rev.,* **110**, 354-384.

Schlax, M. G., D. B. Chelton, and M. H. Freilich, 2000: The effects of sampling errors in wind fields constructed from single and tandem scatterometer datasets. *J. Atmos. Oceanic Technol.*, submitted.

Servain, J., J. N. Stricherz, and D. M. Legler, 1996: TOGA pseudo-stress atlas 1985-1994. vol. I: Tropical Atlantic. *Centre ORSTOM*, Plouzané, France, 158 pp.

Shanno, D. F., and K. H. Phua, 1980: Remark on Algorithm 500 – A variable method subroutine for unconstrained nonlinear minimization. *ACM Trans. Math. Software*, **6,** 618-622.

Siefridt, L., B. Barnier, D. M. Legler, and J. J. O’Brien, 1998: 5-day average winds over the North-West Atlintic from ERS1 using a variational analysis. *Global Atmos. and Ocean Sys*. **5**, 317–344.

Stricherz, J. N., D. M. Legler, and J. J. O’Brien, 1997: TOGA pseudo-Stress atlas 1985-1994: II Tropical Pacific Ocean. *COAPS Rep. 97-2*, 177 p. [Available from COAPS, The Florida State University, Tallahassee FL 32306].

Tang, W. and W. T. Liu, 1996: Objective interpolation of scatterometer winds. *JPL Tech. Rep. 96-19*, 16 p. [Available from Jet Propulsion Laboratory, California Institute of Technology, Pasadena, CA 91109].

Verschell, M. A., M. A. Bourassa, D. E. Weissman, and J. J. O’Brien, 1999: Model validation of the NASA Scatterometer winds. *J. Geophys. Res*., **104**, 11,359–11,374.

Wahba, G., and J. Wendelberger, 1980: Some new mathematical methods for variational objective analysis using splines and cross-validation. *Mon. Wea. Rev*., **108,** 1122-1143.

Wikle, C. K., R. F. Millif, and W. G. Large, 1999: Surface wind variability on spatial scales from 1 to 1000 km observed during TOGA COARE. *J. Atmos. Sci*., **56**, 2222-2231.

Wilks, D. S., 1995: *Statistical Methods in Atmospheric Sciences: An Introduction*. International Geophysics Series 59, San Diego, Academic Press, 467 p.

Zeng, L., and G. Levy, 1995: Space and time aliasing structure in monthly mean polar-orbiting satellite data. *J. Geophys. Res*., **100**, 5133-5142.

Table 1. Weights (β_a, β_b) for one day are calculated by cross validation for different grid spacings. The change in the weights for the different grid resolution is less than an order of magnitude, thus allowing for the conclusion that the multigridding technique is valid for this application of cross validation.

Grid Spacing	β_a	β_b
1°	0.00528	0.00772
2°	0.00613	0.00896
3°	0.00904	0.01034
6°	0.00228	0.00221

Table 2. Weights (β_a, β_b) are calculated by cross validation for two sub-regions (midlatitude and tropical) and the whole study region (Pacific Ocean) for two different dates. The small differences show that the weights are nearly independent of space and pseudostress magnitude.

Region	Weights (1/ 5/97)	Weights (6/14/97)
Midlatitude	$1.18\times10^{-4}; 7.29\times10^{-4}$	$3.18\times10^{-3}; 3.98\times10^{-3}$
Tropical	$9.27\times10^{-5}; 8.61\times10^{-4}$	$1.37\times10^{-4}; 9.73\times10^{-4}$
Pacific Ocean	$3.22\times10^{-3}; 8.61\times10^{-4}$	$2.01\times10^{-4}; 1.36\times10^{-3}$

Table 3. Average specific kinetic energy for the Pacific basin expressed as the average magnitude of the pseudsostress (m^2s^{-2}). The kinetic energy of the derived NSCAT field is close in magnitude to the observations and higher than the kinetic energy for NCEP.

Gridded Product	January 25, 1997	March 16, 1997	June 25, 1997
Derived NSCAT field	28.5	23.3	23.3
NSCAT Observations	29.9	24.2	23.1
NCEP Reanalysis	25.3	20.7	19.8

FIG. 1. 24 hours (May 15, 1997) of NSCAT observations for the Pacific Ocean basin north of 40°S. Observation are binned into a 1° by 1° grid. Vorticity is contoured, and wind vectors are plotted every 3° by 3° for clarity. Gaps in the daily coverage are clearly seen.

FIG. 2. Flow chart for Direct-Minimization. Italics indicate numerical values or results, boxes with double-lined borders indicate input values. Dashed lines indicate a single (initial) use of the input data, and dotted lines indicate repeated use of the input data. There are ~250,000 NSCAT vector wind observations in the study region for each day (~550,000 globally), and ~14,000 water grid points (or ~33,000 globally) for 1° grid spacing. The conjugate gradient method requires the derivative of the functional, for each of these grid points, with respect to both components of the pseudostress vector, for typically eight to ten iterations.

Fig. 3. Flow chart for cross validation and multigridding. Lines and boxes are as for Fig. 2, and the dotted box contains the cross validation procedure. Cross validation must be applied to each weight, typically for six to eight iterations on the coarse grid, and then for one more adjustment on the fine grid. Calculation of the cross validation functional requires $2K+1$ calculations of the direct minimization functional, where K is the number of masked regions.

FIG. 4. Time series of the weights for the smoothing of the pseudostress (a), and smoothing of the curl of the pseudostress (b) constraints determined by cross validation. Weights are valid for the entire Pacific Ocean study region and are calculated roughly every five days (indicated by squares). No pattern or trend is apparent, and the average values (dashed lines) are used for the entire NSCAT period.

FIG. 5. Mean energy density spectra at four latitudes, averaged from Jan. 17, 1997 to March 3, 1997. The slope of the calculated spectra (solid lines) is similar to the slope found in previous studies of scatterometer winds (dashed lines).

FIG. 6. Mean pseudostress of the equatorial cold tongue region for the NSCAT period from the objectively derived NSCAT pseudostress fields. This mean is removed prior to the CEOF analysis. The Northeast and Southeast trade winds are apparent, as well as the gap flow through the Sierra Madres (upper right hand corner).

FIG. 7. A Scree diagram showing the percent variance associated with the first 25 modes of the CEOF analysis. The first four modes are statistically significant.

FIG. 8. Principal Component 1 contains 20.44% of the variance. The spatial function (a) multiplied by the amplitude of the eigenvector (b) gives the magnitude of the pseudostress. Rotation angle (c) is a counterclockwise rotation of the spatial function vectors. Gaps in the time series indicate days that were excluded from the CEOF analysis due to missing data.

FIG. 9. Spectral analysis of the eigenvector amplitude for principal components 1 (a), 2 (b), 3 (c) and 4 (d). Power is plotted against period in days (in an area preserving plot). Confidence limits (90%) are shown as the dashed lines. The spectrum is smoothed using a five point running mean. The time period analyzed is Oct. 25, 1996 – June 29, 1997. Data before Oct. 25 had numerous missing days and are omitted from the spectral analysis. One other missing day (Jan. 16) in the time series is linearly interpolated.

FIG. 10. Rotary spectra for the complex eigenvectors of principal components 1 (a), 2 (b), 3 (c) and 4 (d). Power is plotted against rotation period in days (in an area preserving plot). Confidence intervals (90%) are shown as dashed lines. Positive (negative) periods indicate counterclockwise (clockwise) rotation.

FIG. 11. As for Fig. 8, except for the second principal component has of 10.63% of the variance.

FIG. 12. Spectral analysis of TAO buoy data located at 8°S, 170°W. Pseudostress magnitude (a), and rotary wind spectra (b). Power is plotted against period in days, and is smoothed using a five point running mean. Time period analyzed is the same as Fig. 9 (10/25/96 – 6/29/97), with missing days linearly interpolated. A period of near 20 days (a) matches the result of the spectral analysis of the second principal component's eigenvector (Fig. 9b), and a counterclockwise rotation (positive period) of near 80 days (b) matches the second principal component's rotary spectrum (Fig. 10b).

FIG. 13. As for Fig. 6, except for the third principal component which has 6.56% of the variance.

FIG. 14. As for Fig. 6, except for the fourth principal component, which has 5.69% of the variance.

FIG. 15. Same as Fig. 9, except the TAO buoy was located at 5°S, 125°W. Magnitude of pseudostress (a) shows a period near 7 days and a period between 30 and 50 days that are similar to the periods of the fourth principal component's eigenvector (Fig. 9d). Rotary wind spectrum (b) shows an annual signal and a signal near 40 to 80 days with counterclockwise rotations, which is also found in the fourth principal component's rotary spectrum (Fig. 10d).

FIG. 16. November 1996 mean pseudostress for the objectively derived NSCAT fields (1° by 1° resolution) adjusted to a height of 20 m (a), vectors are plotted every 2° by 2° for clarity. FSU winds monthly pseudostress (2° by 2° resolution) valid for the same time (b). Magnitude of the pseudostress is contoured and direction is indicated by vectors. Magnitudes of the two products are similar but the NSCAT product has finer detail such as the flow off of Central America and the cross equatorial flow in the eastern Pacific.

FIG. 17. Same as Fig. 16 except for May 1997. NSCAT product (a) shows high values of pseudostress off of the coast of Australia which are missing in the FSU wind analysis (b).

FIG. 18. Objectively derived NSCAT winds (a) and NCEP reanalysis (b) for March 16, 1997. Wind component are interpolated to a 1° by 1° grid and vorticity is contoured. Wind vectors are plotted on a 3° by 3° grid for clarity. The NSCAT product has stronger trade winds and stronger winds off of the coast of Central America. NSCAT also shows more detail of storms than NCEP.